

# Star formation efficiency and scaling relations in parsec-scale cluster-forming clumps

Vineet Rawat,<sup>1,2\*</sup> M. R. Samal,<sup>1</sup> A. Zavagno,<sup>3,4</sup> Sami Dib,<sup>5</sup> Davide Elia,<sup>6</sup> J. Jose,<sup>7</sup> D.K. Ojha,<sup>8</sup> K. Srivastav<sup>1,2</sup>

<sup>1</sup>Physical Research Laboratory, Navrangpura, Ahmedabad, Gujarat 380009, India

<sup>2</sup>Indian Institute of Technology Gandhinagar Palaj, Gandhinagar 382355, India

<sup>3</sup>Aix Marseille Univ, CNRS, CNES, LAM Marseille, France

<sup>4</sup>Institut Universitaire de France, 1 rue Descartes, 75005 Paris, France

<sup>5</sup>Max-Planck-Institut für Astronomie, Königstuhl 17, 69117, Heidelberg, Germany

<sup>6</sup>Istituto di Astrofisica e Planetologia Spaziali, INAF, Via Fosso del Cavaliere 100, I-00133 Roma, Italy

<sup>7</sup>Indian Institute of Science Education and Research (IISER) Tirupati, Rami Reddy Nagar, Karakambadi Road, Mangalam (P.O.), Tirupati 517 507, India

<sup>8</sup>Department of Astronomy and Astrophysics, Tata Institute of Fundamental Research, Mumbai 400005, India

16 May 2025

## ABSTRACT

Numerical simulations predict that clumps ( $\sim 1$  pc) should form stars at high efficiency to produce bound star clusters. We conducted a statistical study of 17 nearby cluster-forming clumps to examine the star formation rate and gas mass surface density relations (i.e.  $\Sigma_{\text{SFR}}$  vs.  $\Sigma_{\text{gas}}$ ) at the clump scale. Using near-infrared point sources and *Herschel* dust continuum analysis, we obtained the radius, age, and stellar mass for most clusters in the ranges 0.5–1.6 pc, 0.5–1.5 Myr, 40–500  $M_{\odot}$ , respectively, and also found that they are associated with  $\Sigma_{\text{gas}}$  values ranging from 80–600  $M_{\odot} \text{ pc}^{-2}$ . We obtained the best-fit scaling relations as  $\Sigma_{\text{SFR}} \propto \Sigma_{\text{gas}}^{1.46}$  and  $\Sigma_{\text{SFR}} \propto (\Sigma_{\text{gas}}/t_{\text{ff}})^{0.80}$  for the studied sample of clumps. Comparing our results with existing scaling relations at cloud and extragalactic scales, we found that while the power-law exponent obtained in this work is similar to those found at these scales, the star formation rate surface densities are relatively higher for similar gas mass surface densities. From this work, we obtained instantaneous median star formation efficiency (SFE) and efficiency per free-fall time ( $\epsilon_{\text{ff}}$ ) of  $\sim 20\%$  and  $\sim 13\%$ , respectively, for the studied clumps. We discuss the cause of the obtained high SFE and  $\epsilon_{\text{ff}}$  in the studied clumps and also discuss the results in the context of bound cluster formation within molecular clouds. We conclude that our results do not favour a universal scaling law with a constant value of  $\epsilon_{\text{ff}}$  in star-forming systems across different scales.

**Key words:** ISM: clouds; galaxies: star formation; galaxies: star clusters: general; stars: luminosity function, mass function

## 1 INTRODUCTION

The processes which regulate the conversion of gas into stars are still least understood in molecular clouds, and so is the cluster formation process. To understand the formation of stellar clusters, it is required to follow the sequence of interstellar processes from molecular clouds (MCs) to clumps ( $\sim 1$  pc) and cores ( $\leq 0.1$  pc). However, in reality, this sequential process of star formation is much more complex, involving filamentary structures of MCs and the relative role of gravity, turbulence, magnetic field, and stellar feedback that also varies with the scale size, i.e. from clouds to cores (Krumholz et al. 2014; Krause et al. 2020; Pineda et al. 2022; Hacar et al. 2023; Rawat et al. 2024b). Along with the aforementioned factors, the radiation pressure from newly formed stars (acting mostly on dust) or enhanced thermal pressure from photoionized regions can halt the mass accretion to the clump or core, thereby affecting their outcome (Krumholz et al. 2019). So, inquiring about the star formation rate

(SFR) and how it changes at different stages of cloud evolution and spatial scale is a topic of interest, as it is essential to develop a complete and universal description of star formation in the Galaxy. In short, the quest is to understand whether star formation is regulated by some large galactic scale process or dominated by the local conditions of the star-forming gas material in the region (Dib et al. 2012; Eden et al. 2015; Zhou et al. 2025).

Stars form in groups, deeply embedded within dense clumps of molecular gas. The fate of a nascent stellar system, whether to become an expanding association or to remain a bound cluster, is determined by how rapidly and effectively it disperses the gas material of the clump/cloud. This process is controlled primarily by two parameters: the efficiency of star formation and the timescale on which the remaining gas is disrupted. It is suggested that, if the gas removal is rapid relative to the free-fall time, then more than half the mass must be in stars for the cluster to remain bound (Hills 1980). On the other hand, a sufficiently slow mass loss allows a virialized stellar system to expand adiabatically and remain bound. Simulations suggest that the star formation efficiency (SFE) within the cluster-forming

\* E-mail: vinitrawat1996@gmail.com

region impacts the emergence of a rich and bound cluster (Goodwin & Bastian 2006; Dib et al. 2011; Dib et al. 2013; Geen et al. 2017; Shukirgaliyev et al. 2017; Grudić et al. 2018; Krumholz et al. 2019; Li et al. 2019). In addition, it is also suggested that the primordial gas mass, structure, and density profile also plays a decisive role in massive stars and associated cluster formation (e.g. Bonnell & Bate 2006; Parker et al. 2014; Chen et al. 2021). To investigate how the amount of total gas scales with the total number of stars formed, it is important to quantify the SFR and SFE of a star-forming region and understand their correlations with time scales as well as spatial scales.

The connection between the SFR and the gas mass is known as the star formation scaling laws. Schmidt (1959) established, for the first time, that the SFR density is proportional to the square of the density of the gas. Kennicutt (1998b) investigated a global Schmidt law by measuring the projected star formation rate surface densities ( $\Sigma_{\text{SFR}}$ ) and gas mass surface densities ( $\Sigma_{\text{gas}}$ ) of 61 normal galaxies using  $\text{H}\alpha$ ,  $\text{H I}$ , and CO observations. This relation at the extragalactic scale is popularly known as the Kennicutt-Schmidt (KS) relation:

$$\Sigma_{\text{SFR}} = (2.5 \pm 0.7) \times 10^{-4} \left( \frac{\Sigma_{\text{gas}}}{1 \text{M}_{\odot} \text{pc}^{-2}} \right)^{1.4 \pm 0.15} \times (\text{M}_{\odot} \text{yr}^{-1} \text{kpc}^{-2}). \quad (1)$$

Although large-scale studies offer crucial insights into the correlation between the overall properties of galaxies and the formation of stars, the gas conversion into stars occurs however at a more localized level, i.e. in MCs, down to much smaller scales (clumps and cores). Studying the scaling relations in the MCs of our own Milky Way Galaxy offers the advantage of higher resolution than any other extragalactic clouds. Therefore, the clouds and the sub-structures within them, along with the stars, can be better resolved and studied at various scales. The earlier studies on scaling relations for MCs in the Milky Way show higher slopes and  $\Sigma_{\text{SFR}}$  values than the KS relation, as well as broad distribution in the  $\Sigma_{\text{SFR}}$  and  $\Sigma_{\text{gas}}$  plot (Evans et al. 2009; Lada et al. 2010; Heiderman et al. 2010; Kennicutt & Evans 2012; Lada et al. 2013; Evans et al. 2014). For example, Evans et al. (2009) and Heiderman et al. (2010) studied the SFR–gas mass relation for a sample of nearby low-mass Galactic molecular clouds using the Spitzer Cores to Disks (c2d) and Gould Belt (GB) survey data, respectively, and found that the SFRs in these Galactic clouds lie almost 20–30 times above the KS relation.

Krumholz et al. (2012) argued that  $\Sigma_{\text{SFR}}$  is better correlated with  $\frac{\Sigma_{\text{gas}}}{t_{\text{ff}}}$ , than  $\Sigma_{\text{gas}}$  itself, where  $t_{\text{ff}}$  is the free-fall time-scale of the considered system. The relation between  $\Sigma_{\text{SFR}}$  and  $\frac{\Sigma_{\text{gas}}}{t_{\text{ff}}}$  is known as volumetric relation and is expressed as:

$$\Sigma_{\text{SFR}} = \epsilon_{\text{ff}} \frac{\Sigma_{\text{gas}}}{t_{\text{ff}}}, \quad (2)$$

where  $\epsilon_{\text{ff}}$  is known as the star-formation efficiency per free-fall time and is a dimensionless measure of the SFR. (Krumholz et al. 2012) find the best fitted value for  $\epsilon_{\text{ff}}$  to be around 0.01 for data involving molecular clouds in the solar neighbourhood, Local Group galaxies, unresolved disks, and starburst galaxies in the local and high-redshift universe. Krumholz et al. (2012) advocates for a universal star formation law across all scales, in which molecular clouds as well as galaxies as a whole convert their mass into stars at a rate of  $\sim 1\%$  of the mass per free-fall time.

Evans et al. (2014) tested the volumetric star formation relation for 29 nearby MCs compiled from the Spitzer c2d and GB survey data, and argued that involving free-fall time does not reduce the scatter

in  $\Sigma_{\text{SFR}} - \Sigma_{\text{gas}}$  relation. Evans et al. (2014) suggest that  $\epsilon_{\text{ff}} = 0.01$  does not predict the behavior of SFRs on small scales within MCs. Pokhrel et al. (2020, 2021) re-investigated the scaling relations in 12 nearby MCs and within single clouds using the Spitzer Extended Solar Neighborhood Archive (SESNA) catalogue (Gutermuth et al. 2019) and found a good correlation between  $\Sigma_{\text{SFR}}$  and  $\Sigma_{\text{gas}}$ . The authors also showed that the correlation becomes even stronger by including the free-fall time scale in the relation. Overall, the power-law exponent of the  $\Sigma_{\text{SFR}} \propto \Sigma_{\text{gas}}^N$  relation changes from 1.0–1.5 at extragalactic scales (Bigiel et al. 2008; Kennicutt & Evans 2012; de los Reyes & Kennicutt 2019) to 1.5–2.0 at molecular cloud scales (Gutermuth et al. 2011; Lada et al. 2013; Evans et al. 2014; Das et al. 2021; Pokhrel et al. 2021). It is worth noting that these scaling relations are derived using different methodologies and data sets (Table 1) and thus are sensitive to adopted methodologies and data quality. For example, recent high-resolution magnetohydrodynamic numerical simulations by Suin et al. (2024) show that the sensitivity and resolution of observations play a significant role in setting the scaling relations. Simulations also suggest various star formation proxies can systematically over- and under-estimate the actual instantaneous  $\epsilon_{\text{ff}}$  at different times (Grudić et al. 2022).

It is believed that the majority of stars in a MC, if not all, form in star clusters (Lada & Lada 2003). In MCs, the clumps are the actual sites where clusters form, and cores are the sites where individual stars form. Therefore, it is crucial to examine the behaviour of scaling relations from cloud-to-clump-to-core scales for a deeper understanding of the key processes that govern and regulate the formation of stars. In addition, understanding the SFR–gas mass scaling relations over different spatial scales is important for the evolution of the SFRs and SFEs from MCs to cores via clumps. However, very few studies on the scaling relations at the clump scale have been done so far (e.g. Heyer et al. 2016). In this work, we extend the studies on star formation scaling relations to clump scale by measuring the star formation properties of a sample of clumps hosting embedded clusters (see Section 2) that are visible in near-infrared (NIR). We then discuss the obtained results in the context of star and star cluster formation in molecular clouds. This work is organized as follows: The data sets and sample selection are presented in Section 2. The results are presented and discussed in Section 3. In Section 4, we discuss the obtained scaling relations, as well as the SFE and SFR, with respect to the values obtained over various scales, and we also discuss the results in the context of cluster formation. In Section 5, we summarize our work with concluding remarks.

## 2 DATA USED AND SAMPLE SELECTION

To determine the properties of embedded clusters, NIR photometric data ( $J$ ,  $H$ , and  $K$ ) from the UKIDSS’s Galactic Plane Survey (GPS; Lucas et al. 2008) of DR10 was used in this work. This survey was done using the Wide Field Camera (WFCAM; Casali et al. 2007) mounted on the United Kingdom Infra-Red Telescope (UKIRT) 3.8-m telescope. The WFCAM has 4 Rockwell Hawaii-II 2048  $\times$  2048 HgCdTe detectors with a pixel scale of  $\sim 0.4''$ , and have broadband ZYJHK filters and narrowband H2 and Bry filters (Casali et al. 2007). The GPS survey has a resolution of around 1 arcsec and a typical depth of 19.8, 19.0, and 18.1 mags in the  $J$ ,  $H$ , and  $K$  bands, respectively. In this work, only those point sources were used which have an error of less than 0.1 mag in all three bands. For sources brighter than the saturation limits of the UKIDSS GPS data, i.e.  $J = 13.25$ ,  $H = 12.75$ , and  $K = 12.0$  mag (Lucas et al. 2008), the

**Table 1.** Summary of scaling relations.

Reference	Scale size (pc)	SFR tracer	Gas mass tracer	$\Sigma_{\text{SFR}} \propto \Sigma_{\text{gas}}^N$ ; $N$
<a href="#">Kennicutt (1998b)</a>	extragalactic	H $\alpha$	H I + CO	$1.40 \pm 0.15$
<a href="#">Bigiel et al. (2008)</a>	extragalactic ( $\sim 750$ )	<i>Spitzer</i> mid-IR and FUV maps	H I + CO	$1.0 \pm 0.2$
<a href="#">Evans et al. (2009)</a>	3–10 ( $\sim 6$ ) <sup>a</sup>	<i>Spitzer</i> c2d	Extinction maps (c2d and 2MASS; 240'')	—
<a href="#">Heiderman et al. (2010)</a>	1.75–15 ( $\sim 5.4$ )	<i>Spitzer</i> c2d and GB	Extinction maps (c2d and 2MASS; 270'')	—
<a href="#">Heiderman et al. (2010)</a> (clumps)	0.26–11 ( $\sim 2.26$ )	Total IR luminosity	HCN (J=1–0)	1.0
<a href="#">Lada et al. (2010)</a>	6–66 ( $\sim 28$ )	<i>Spitzer</i> c2d	Extinction maps (2MASS)	—
<a href="#">Evans et al. (2014)</a>	1–15 ( $\sim 4.3$ )	<i>Spitzer</i> c2d and GB	Extinction maps (c2d and 2MASS; 270'')	—
<a href="#">Heyer et al. (2016)</a>	0.15–10.5 ( $\sim 1.5$ )	<i>Spitzer</i> MIPS GAL survey 24 $\mu$ m	ATLAS GAL 870 $\mu$ m and NH <sub>3</sub> line emission	—
<a href="#">Pokhrel et al. (2021)</a>	11.5 $\times$ 12.0–142.2 $\times$ 163.7	SESNA catalog	<i>Herschel</i> maps	2.0
<a href="#">Elia et al. (2025)</a>	2000 (Milky Way)	70 $\mu$ m luminosity (Hi-GAL survey)	CO	$1.10 \pm 0.06$

Note: <sup>a</sup> The values quoted in the brackets are the mean scale sizes of the studied regions.

photometric values from the Two Micron All-Sky Survey (2MASS) NIR data are used ([Cutri et al. 2003](#)).

Since for measuring the SFR and SFE, both stellar mass and gas mass are to be estimated, we thus selected clusters that are visible in NIR and are also associated with cold dust. In NIR, although 2MASS has provided a point source catalogue over the whole sky, deep NIR GPS survey, covers mostly the Galactic plane. Similarly, sensitive cold dust continuum images are available for the Galactic plane from the *Herschel* Infrared Galactic Plane Survey (Hi-GAL; [Molinari et al. 2010](#)). Therefore, in order to adopt a homogeneous approach for estimating stellar and dust properties, we restrict our sample to the Galactic plane within  $-2^\circ < b < 2^\circ$  encompassing these surveys. We also restrict our sample in the longitude range,  $60^\circ < l < 240^\circ$ , to avoid sources in the Galactic bulge direction due to high field star densities and high interstellar extinction that would affect the determination of the cluster properties. We search for the embedded cluster sample by simultaneously looking at NIR and far-IR Galactic plane images using the ALADIN software ([Baumann et al. 2022](#)). While searching, we also consider that the clusters should not be part of a highly structured dusty environment for better estimation of their boundaries and, thus, their properties. Therefore, our sample is biased to those clusters that are largely situated in isolated cold clumpy structures, although in some cases, the clusters are found to be connected to extended structures in their outskirts. In addition, we restrict the cluster sample to be within 2.5 kpc, which is primarily based on the mass sensitivity limit of the GPS survey. We aimed to detect point sources down to at least  $0.5 M_\odot$  at 2.5 kpc with the typical data completeness of the GPS survey, so that we can estimate the total stellar mass of the cluster by extrapolating to lower masses (i.e.  $\sim 0.1 M_\odot$ ) using the functional form of the initial mass function (IMF). Given that the typical median visual extinctions of young clusters, ranging from a parsec to a few parsecs in size and aged  $\sim 0.5$  to 2 Myr, fall within 3 to 15 mag (see Fig. 9 of [Rawat et al. 2024a](#)), we estimate that with the typical data completeness of the GPS survey ([Lucas et al. 2008](#)) at *K*-band, we would be able to detect  $0.5 M_\odot$  sources up to 2.5 kpc. This detection limit holds even in regions with  $A_V = 20$  mag for clusters as young as 0.5 Myr. Since

the clusters are associated with cold dust in the *Herschel* SPIRE bands and are also either barely visible or invisible in optical images such as DSS-2 and Pan-STARRS, most of the clusters in our sample are expected to be young. Thus, our initial estimate of an age of 0.5–2 Myr seems to be a reasonable assumption. We discuss more on the age estimation in Section 3.3. With the aforementioned selection criteria, our final sample consists of 17 clusters in the distance range of 1.5 to 2.2 kpc, which are listed in Table 2.

For estimating the gas mass of the clumps (see Section 3.4), we used the *Herschel* column density ( $N(\text{H}_2)$ ) maps of the clumps made with the PPMAP technique by [Marsh & Whitworth \(2019\)](#). The PPMAP-based column density maps are constructed using the far-infrared images of the Hi-GAL survey and are available<sup>1</sup> for the entire Galactic plane within a strip of around 2 degrees in latitude. The Hi-GAL data is taken with the *Herschel* PACS and SPIRE instruments at wavelengths 70, 160, 250, 350, and 500  $\mu$ m with angular resolutions of 8.5, 13.5, 18.2, 24.9, and 36.3'', respectively ([Molinari et al. 2010](#)). The PPMAP provides the resolution of 12'' that corresponds to the spatial resolution of  $\sim 0.08$ – $0.13$  pc for the clumps studied in this work.

### 3 ANALYSIS AND RESULTS

The present-day SFE is defined as the ratio of the total stellar mass ( $M_*$ ) to the total mass of a star-forming region, i.e. stellar mass plus present-day gas mass ( $M_* + M_{\text{gas}}$ ). The SFR is calculated as,  $M_*/t_{\text{clust}}$ , where  $t_{\text{clust}}$  is the age of the cluster. The identification and counting of young stellar objects (YSOs) and using the information of their average mass and lifetimes is a direct way to quantify the SFR, which is known as the star-count method. In most of the previous studies, the star-count method was mostly employed for nearby clouds ( $< 1$  kpc) (e.g.; [Evans et al. 2009](#); [Heiderman et al. 2010](#); [Lada et al. 2010](#)) due to the low sensitivity of the *Spitzer* data at larger distances. It is suggested that employing average mass and time over molecular

<sup>1</sup> [http://www.astro.cardiff.ac.uk/research/ViaLactea/PPMAP\\_Results/](http://www.astro.cardiff.ac.uk/research/ViaLactea/PPMAP_Results/)

**Table 2.** Sample of clusters.

No	Name	GLON (degree)	GLAT (degree)	$D$ (kpc)	Ref.
1	IRAS 06063+2040	189.859	0.502	$2.10 \pm 0.42$	1
2	IRAS 06055+2039	189.769	0.336	$2.10 \pm 0.42$	1
3	IRAS 06068+2030	190.053	0.538	$2.10 \pm 0.42$	1
4	IRAS 22134+5834	103.875	1.856	$1.50 \pm 0.30^*$	2
5	IRAS 06056+2131	189.030	0.784	$1.76 \pm 0.35$	1
6	Sh2-255 IR	192.601	-0.047	$1.96 \pm 0.12$	3
7	[IBP2002] CC14	173.503	-0.060	$1.80 \pm 0.36$	1
8	IRAS 06058+2138	188.949	0.888	$1.76 \pm 0.35$	1
9	IRAS 06065+2124	189.232	0.895	$2.00 \pm 0.40^*$	4
10	NGC 2282	211.239	-0.421	$1.70 \pm 0.40$	5
11	IRAS 05490+2658	182.416	0.247	$2.20 \pm 0.44$	1
12	BFS 56 IR	217.373	-0.080	$2.10 \pm 0.42^*$	6
13	Sh2-88	61.472	0.095	$2.06 \pm 0.08$	3
14	IRAS 06103+1523	194.931	-1.210	$2.00 \pm 0.40^*$	2
15	IRAS 06104+1524A	194.926	-1.194	$2.00 \pm 0.40^*$	2
16	IRAS 06117+1901	191.916	0.822	$2.20 \pm 0.44$	1
17	IRAS 05480+2545	183.348	-0.576	$2.10 \pm 0.42^*$	7

References: [1] Mège et al. (2021), [2] Maud et al. (2015), [3] Méndez-Delgado et al. (2022), [4] Dutra & Bica (2001), [5] Dutta et al. (2015), [6] Elia et al. (2013), and [7] Henning et al. (1992). Note: \* For clusters without reported distance errors in the literature, we have assumed an average uncertainty of around 20%.

cloud scale may not be entirely accurate when star formation is not uniform in time (Dib et al. 2025). For distant star-forming regions, indirect tracers of the SFR are used like  $H\alpha$  emission, ultraviolet continuum, infrared luminosities, and radio continuum emission (see the review article by Kennicutt 1998a; Kennicutt & Evans 2012).

In this work, we explore the star formation properties of a sample of cluster-forming regions of typical size around 1 pc. Below, we present the analysis steps that we applied to all the clusters in our sample by showcasing the steps for an exemplary cluster, i.e. IRAS 06063+2040. Fig. 1a-b shows the 3-color RGB image of IRAS 06063+2040 in  $JHK$  bands from 2MASS and UKIDSS. Fig. 1c shows the *Herschel* 500  $\mu\text{m}$  image of IRAS 06063+2040, showing the presence of cold dust in the cluster region. As can be seen, point sources in the UKIDSS images are more resolved and richer compared to the 2MASS images, and the distribution of 500  $\mu\text{m}$  emission around the cluster suggests that the cluster is associated with cold dust.

### 3.1 Extent of the cluster

In comparison to open clusters, defining the centre of young clusters is much more difficult due to variable high extinction, nebulosity, and complex shapes. For assessing the shape and size of the cluster, we selected data for a larger region around the geometric centre of the cluster and plotted a 2-dimensional kernel density estimate (KDE) map with a bin width of 0.5 to 0.7. The region for making the KDE map is selected in such a way that there should be an ample number of stars to make a smoothed KDE map of the cluster. The optimum bin width was chosen to have a good compromise between over- and under-smoothing density fluctuations, depending upon the data statistics in the cluster region. Then, we find the peak density point using Gaussian KDE and choose these coordinates as the approximate centre of the cluster. Fig. 2a shows the 2D density plot of IRAS 06063+2040 with its peak density point marked with a cross sign.

To determine the effective radius of the cluster ( $R_{\text{clust}}$ ), we constructed its radial density profile (RDP). To do this, we first divided the cluster into different annular rings from the centre. The radius of the annular rings from the centre was defined by the auto-binning option of the Pyplot module in Matplotlib. Then, we counted the stars in each radial bin and calculated the stellar density in each annulus by dividing the total counts with the area of the annulus. Fig. 2b shows the plot of stellar density as a function of radius for IRAS 06063+2040. In order to obtain the radius of the cluster, we fitted the RDP with the empirical King’s profile (King 1962) of the form

$$\rho(r) \propto b_0 + \frac{\rho_0}{\left[1 + \left(\frac{r}{r_c}\right)^2\right]}, \quad (3)$$

where  $b_0$ ,  $\rho_0$ , and  $r_c$  are the background stellar density, peak stellar density, and core radius of the cluster, respectively. The King’s profile fit to the stellar density of IRAS 06063+2040 is shown in Fig. 2b, and the background stellar density is shown by a solid blue line. The radius of the cluster is defined as the radial distance at which the modelled stellar density lies  $5\sigma$  above the background stellar density. For example, Fig. 1a and b also shows the outer extent of the IRAS 06063+2040 cluster on the UKIDSS and 2MASS images. As can be seen from the images, the stellar density beyond the cluster boundary is very low and indistinguishable from the background density, implying that the chosen cluster radius above  $5\sigma$  of the background is a reasonable choice.

For some clusters, we found that King’s profile does not completely become flattened at the background stellar density, either due to low statistics or confusion with other nearby stellar groups/clusters. In such cases, we choose an optimum value from the 2D stellar density map and also by visually inspecting the UKIDSS NIR images. The radius of all the clusters is given in Table 3 and lies in the range of 0.5 to 1.6 pc.

The photometric data can be incomplete towards the fainter end in the clustered environment due to stellar crowding and a bright background. To determine the completeness of the UKIDSS NIR data within the cluster radius, the histogram turnover method was used (for details, see Damian et al. 2021; Rawat et al. 2024a, and references therein). This approach allows a determination of the approximated completeness limits. With this approach, the completeness limit for most clusters within the cluster radius was found to be in the ranges 17.1–18.3, 15.9–17.5, and 15.6–16.8 mag in the  $J$ ,  $H$ , and  $K$  bands, respectively.

### 3.2 Extinction

For deriving cluster properties, the contributions of field stars and extinction in the direction of the cluster need to be determined. To assess extinction toward the cluster, following the commonly adopted approach (e.g. Gutermuth et al. 2008, 2009), a control field region near the cluster location that is relatively dust-free was selected to evaluate the median intrinsic colors of field stars in the cluster’s direction. Large control fields with a radius of around 5–7 arcmin were used to get better statistics of the field population. The photometric data of the control fields was selected in the same way as done for the cluster sample. We then estimated the visual extinction ( $A_V$ ) of the observed stars projected within the cluster radius using the following equation and using the mean  $J - H$  and  $H - K$  colors of the control field sources as the intrinsic colors of the stars:

$$A_V = c \times [(i - j) - (i - j)_0]; \quad i \text{ and } j = J, H, \text{ and } K, \quad (4)$$

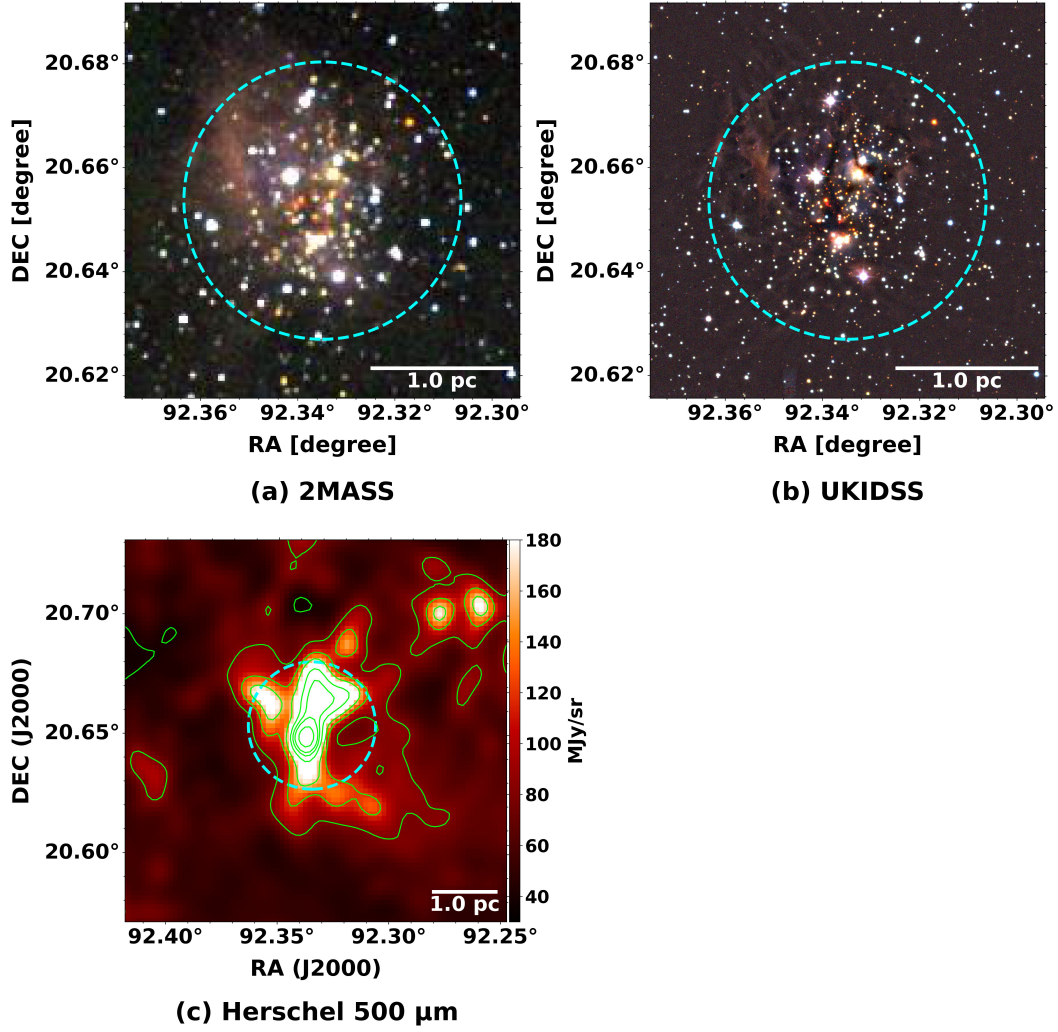


**Figure 1.** (a) 2MASS and (b) UKIDSS NIR color-composite (Red:  $K$  or  $K_s$  band for 2MASS; Green:  $H$  band, and Blue:  $J$  band) image of IRAS 06063+2040. The cyan dashed circle shows the extent of the cluster (see Section 3.1). (c) The *Herschel* 500  $\mu\text{m}$  image of IRAS 06063+2040 along with contour levels at 20, 40, 80, 120, 160, 240, 320, 400, and 600 MJy/sr.

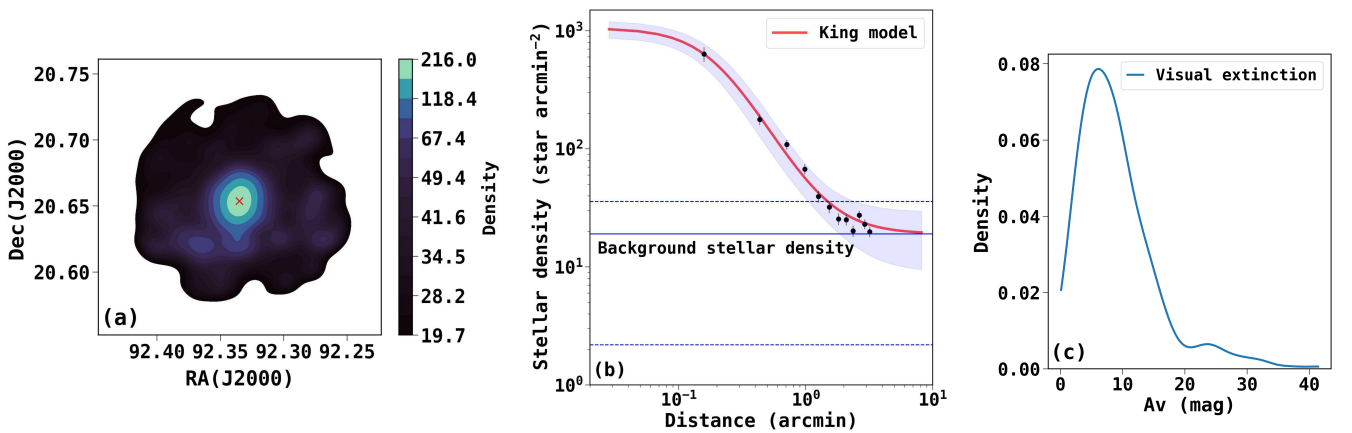


**Figure 2.** (a) A 2D density plot of the stellar distribution observed in the direction of the IRAS 06063+2040 cluster, with the cross symbol indicating the cluster centre taken at the peak density point. (b) The observed stellar surface density of IRAS 06063+2040 as a function of distance from the centre (cross symbol in panel-a). The red curve shows the best fit King's profile along with  $3\sigma$  uncertainty as blue shaded region. The error bars at each point represent the Poisson uncertainties. The solid blue line shows the best-fit background stellar density with  $5\sigma$  uncertainty as blue dashed lines. (c) Density plot of visual extinction of all the sources observed towards the direction of IRAS 06063+2040.

where the mean color of the control field sources  $(i-j)_0$  is subtracted from the observed colors of the stars  $(i-j)$ . Here,  $c$  is the constant whose value is taken to be 9.34 and 15.98 for the  $J-H$  and  $H-K_s$  color excesses, respectively, by adopting the [Rieke & Lebofsky \(1985\)](#) extinction laws. We then derived the median extinction of the cluster following the method adopted in [Rawat et al. \(2024a\)](#). Fig. 2c shows the density plot of visual extinction for IRAS 06063+2040. We find that the median  $A_V$  for IRAS 06063+2040 is around  $6.0 \pm 3.1$  mag, with only 6% sources having  $A_V$  greater than 20 mag. Following a similar analysis, we find the median  $A_V$  values for the cluster sample to be in the range of 2 to 11 mag and are given in Table 3.

### 3.3 $K$ -band luminosity function and age estimation

The  $K$ -band luminosity function (KLF) is the distribution of  $K$  band magnitudes of the sources, which can be used to estimate the proxy age of a cluster by matching the KLF of the observed cluster with that of the modelled clusters (for details, see [Rawat et al. 2024a](#), and references therein). Briefly, we adopt the following procedure. The KLF is expressed as:

$$\frac{dN}{dm_K} = \frac{dN}{dM_*} \times \frac{dM_*}{dm_K}, \quad (5)$$

where  $m_K$  and  $M_*$  are the  $K$ -band luminosity and mass of the stars, respectively. In the above equation,  $dN/dm_K$  represents the number of stars within a  $K$ -band magnitude bin,  $dN/dM_*$  corresponds to the underlying stellar mass function, and  $dM_*/dm_K$  describes the mass-luminosity ( $M-L$ ) relation. Thus, to determine the KLF of the cluster, firstly, the contamination of the field stars was removed by subtracting the KLF of the control field population from that of the observed cluster population. We use the same control field discussed in Section 3.2 to assess the field star population in the direction of the cluster. The KLF of the control field is the distribution of the  $K$ -band magnitudes of the field stars reddened by the median  $A_V$  of the cluster region. Fig. 3a shows the KLF of the cluster before field subtraction and the KLF of the reddened control field with the same bin size. Since the size of the control field region is larger than the size of the cluster region, the field sources are first normalized to the cluster size at each bin and then subtracted from the cluster KLF to obtain the field-subtracted cluster KLF, which is also shown in Fig. 3a.

Then, for estimating the age ( $t_{\text{clust}}$ ) of a cluster, we compared the field-subtracted cluster KLF with the modelled KLFs of synthetic clusters at different ages. We used the Stellar Population Interface for Stellar Evolution and Atmospheres (SPiSEA) python code ([Hosek et al. 2020](#)) to generate the synthetic clusters with an age range of 0.1 to 3.0 Myr. The SPiSEA code generates the synthetic clusters based on various input parameters such as initial cluster mass, distance, functional form of the IMF, metallicity, stellar evolution models, atmosphere models, and extinction law (for details, see [Hosek et al. 2020](#)). The code randomly draws the stars from the chosen IMF until the total mass of stars reaches close to the initial cluster mass. We generated synthetic clusters of solar metallicity with photometric magnitudes in the UKIDSS  $J$ ,  $H$ , and  $K$  filters, at the adopted distances of the observed clusters, using the MIST evolutionary models, a composite grid of atmospheric models, the Kroupa IMF, and the Rieke–Lebofsky extinction law ([Rieke & Lebofsky 1985](#)). The code generates all the stars at the same age, depending on the selected isochrone model. Since SPiSEA randomly generates sources for a cluster of a given age, to obtain the median KLF of each age, we ran

the simulation 200 times for each age. We then matched the observed KLF of each cluster with the synthetic KLFs of different ages, as discussed in ([Rawat et al. 2024a](#)).

Fig. 3b shows the KLFs of the synthetic clusters and the field subtracted KLF of IRAS 06063+2040. From the figure, it can be seen that the KLF of IRAS 06063+2040 lies close to the synthetic KLFs of age between 0.5 to 1.0 Myr. Therefore, we considered 0.75 Myr as the approximate age of the IRAS 06063+2040 cluster. Star clusters can exhibit an age spread, which is not accounted for in the SPiSEA model. It is suggested that high-density molecular clumps may yield clusters with smaller stellar age spreads than those formed by low-density clumps, and observations also support this hypothesis that compact clusters tend to exhibit less age spread compared to extended cluster-forming regions ([Parmentier et al. 2014](#), and references therein). This could be the reason that the observed KLF in Fig. 3b is distributed mainly between the 0.5 to 1 Myr KLF of the synthetic clusters. We thus assigned a median age of  $0.75 \pm 0.25$  Myr to IRAS 06063+2040, which also agrees with the age and age dispersion of the cluster obtained through an independent method, which is described below. Following a similar analysis, we determined the ages of all the clusters, which are given in Table 3. The ages of most of the clusters range from 0.5 to 1.5 Myr, suggesting that they are indeed young clusters. We find that for the obtained age and median extinction of the clusters, the  $K$ -band data is largely complete down to  $\sim 0.2 M_\odot$ .

The age of young clusters is a fundamental parameter that is among the most uncertain and difficult to constrain (see [Soderblom et al. 2014](#), for a review). The classic method for estimating the age is through the Hertzsprung–Russell diagram (HRD), where the positions of member stars are compared with the locations of theoretical pre-main sequence evolutionary tracks and isochrones. For embedded clusters, due to variable extinction (e.g. [Getman et al. 2019](#)), this method may work well if spectroscopic measurements are available for a significant number of stars. While for optically visible clusters with insignificant extinction variation, optical color-magnitude diagrams are often used to constrain age (e.g. [Pandey et al. 2013](#); [Jose et al. 2017](#); [Panwar et al. 2017](#)). In the present work, due to the lack of spectroscopic information for the studied sample, we constrained the age of the clusters using KLF modelling. Although KLF modelling is a proxy way for estimating the age, its advantage for embedded clusters is that it accounts for embedded sources in the age determination. For embedded clusters, using an optical HR diagram may bias the estimated cluster age toward older values, as young clusters and star-forming regions often contain stars at various evolutionary stages—ranging from evolved Class III sources to embedded Class I sources (e.g. [Allen et al. 2008](#); [Samal et al. 2015](#); [Povich et al. 2016](#)). Nonetheless, as a sanity check, we determined the age of IRAS 06063+2040 by deriving the stellar properties of the sources through spectral energy distribution (SED) modelling, where we fitted the observed SED with theoretical models to derive the stellar properties and subsequently derived the age of the stars. SED modelling with data points in optical bands better constrains the stellar properties. Therefore, we restrict the SED modelling to sources within the cluster radius that have measurements available in the optical bands, in addition to the infrared (1.0–8  $\mu\text{m}$ ) bands. Doing so, we estimated the median age of the cluster, based on 15 well-fitted sources, to be  $\sim 0.8 \pm 0.4$  Myr, which agrees well with the age derived from the KLF modelling. This close agreement between the methods may be accidental for IRAS 06063+2040, but this analysis suggests that, in the absence of better information on embedded sources, KLF modelling is a reasonable approach for deriving clus-

ter age. The details of the SED modelling and age determination for IRAS 06063+2040 are given in Appendix B.

Moreover, we want to emphasize that the age determination of a MC complex is also scale-dependent, as star formation models of collapsing clouds such as the global hierarchical collapse (GHC; Vázquez-Semadeni et al. 2019) suggest that clouds collapse hierarchically from large-scale to small-scale, forming structures (such as filaments, clumps, and cores) under the influence of global gravity. These models suggest that global gravity results in ever-increasing densities towards the cloud's centre of potential via filamentary flows, resulting in older stars in the extended part of the cloud and young massive stars/clusters in the hub, where filaments merge to form dense and massive clumps (e.g., see discussion in Rawat et al. 2023, 2024c, for observational evidence). In fact, based on photometric analysis, such a core-halo age gradient (e.g. Getman et al. 2018; Panwar et al. 2018) or evolutionary gradient (e.g. Rawat et al. 2023) has been observed in young clusters and molecular clouds, i.e. stars in the core regions are younger than those in the halo or extended regions. All these results imply that the average age of a molecular cloud may differ from the age of the individual cluster-forming clumps. Thus, it is necessary to determine the age of the region of interest for a better estimation of the SFR and SFE.

Based on the error in age estimation for IRAS 06063+2040 (i.e.  $\sim 0.8 \pm 0.4$  Myr) from the SED fitting and the distribution in KLFs of the clusters, in this work, we have adopted an uncertainty of 50% in the age estimation of all the clusters. We note that the ages reported in Table 2 are the present average ages of the clusters within their respective radii.

### 3.4 Gas properties of the clusters

One important term in the scaling relations is the gas mass of the star-forming regions. We calculated the gas mass ( $M_{\text{gas}}$ ) using the *Herschel* column density map and the following equation:

$$M_{\text{gas}} = \mu_{\text{H}_2} m_{\text{H}} A_{\text{pixel}} \Sigma N(\text{H}_2), \quad (6)$$

where  $\mu_{\text{H}_2}$  is the mean molecular weight of the hydrogen molecule that is taken to be 2.8 (Kauffmann et al. 2008),  $m_{\text{H}}$  is the mass of the hydrogen atom,  $A_{\text{pixel}}$  is the area of the pixel, and  $\Sigma N(\text{H}_2)$  is the integrated column density. We estimated  $\Sigma N(\text{H}_2)$  within the clump boundary using PPMAP-based column density maps. Defining the clump boundary in a cloud is a complex problem, as it depends on parameters such as the resolution, tracer, and sensitivity of the observations. High-resolution data leads to more resolved structures, while low-resolution data can lead to massive structures. Similarly, warm tracers generally trace more extended environments, whereas millimetre wavelengths are better suited for tracing cold gas, which is most relevant to star formation. In the present case, since most clusters are of size  $> 0.5$  pc; thus, we search for cold clumps identified with low-resolution (beam  $\sim 33''$ ) 1.1-millimetre data from the Bolocam Galactic Plane Survey (BGPS; Dunham et al. 2011), around the stellar density peak. We found that for six sources, the radii from the BGPS clumps are available and are found to be in close agreement with the corresponding cluster radii. We thus estimate the gas mass of the cluster within the cluster radius. The gas masses of the clumps range from 120 to 1400  $M_{\odot}$  and are given in Table 3. The uncertainty associated with the gas mass of the clumps ranges from 39% to 55%, accounting for uncertainties in the gas-to-dust mass ratio, opacity index, and distance of the clumps (for details, see Rawat et al. 2023). Using  $M_{\text{gas}}$  and  $R_{\text{clust}}$  of the clumps, the molecular gas mass surface

density ( $\Sigma_{\text{gas}}$ ), number density ( $n_{\text{H}_2}$ ), and free-fall time of the clumps are estimated by using the following equations:

$$\Sigma_{\text{gas}} = \frac{M_{\text{gas}}}{\pi R_{\text{clust}}^2}, \quad (7)$$

$$n_{\text{H}_2} = \frac{3M_{\text{gas}}}{4\pi R_{\text{clust}}^3 \mu_{\text{H}_2} m_{\text{H}}}, \quad (8)$$

$$t_{\text{ff}} = \left( \frac{3\pi}{32 G \mu_{\text{H}_2} m_{\text{H}} n_{\text{H}_2}} \right)^{1/2}, \quad (9)$$

where  $G$  is the gravitational constant. All the physical parameters of the clumps are listed in Table 3. We want to point out that for the IRAS 05480+2545 cluster in our sample, the PPMAP-based map shows saturation at high-density regions. Therefore, we used the Hi-GAL column density map from Schisano et al. (2020) (resolution  $\sim 34''$ ) for this particular cluster. We compared the mass estimates derived from the column density maps of PPMAP and Schisano et al. (2020) for cluster FSR 655 (Rawat et al. 2024c), shown here in Fig. 6 and 7. By doing so, we found that the estimated total gas masses from both column density maps are comparable within 20%.

### 3.5 Cluster mass, star formation rate, and efficiency

In this work, we have determined the age of individual clusters using their  $K$ -band luminosity functions. The theoretical mass-luminosity ( $dM_*/dM_K$ ) relation corresponding to the age of a cluster can be matched with its field-subtracted KLF ( $K$ -band magnitude distribution), to obtain the stellar mass distribution of the cluster. Then, the total stellar mass of the cluster can be estimated by integrating its mass distribution function (e.g. see Rawat et al. 2024a). We used the mass-luminosity relations from the MIST stellar evolutionary models of solar metallicity (Choi et al. 2016), and extinction laws of Rieke & Lebofsky (1985) to get the mass distribution corresponding to the KLF. Generally, a mass distribution function is described in the following logarithmic form:

$$\frac{dN(\log M)}{d \log M} \propto M^{-\Gamma}. \quad (10)$$

Although our data is complete above  $0.2 M_{\odot}$  in most cases, to avoid any possible bias that may be introduced at the fainter mass end, we fitted the mass distribution at the high mass end, i.e. mass  $> 0.4 M_{\odot}$  to obtain  $\Gamma$  values. The  $\Gamma$  values of all the clusters are found to be within  $2\sigma$  error of the canonical value of  $\Gamma$ , i.e. 1.3 (Kroupa 2001) for the mass range of  $0.4 M_{\odot} < M < 8 M_{\odot}$ . The  $\Gamma$  value of 1.3 corresponds to the Kroupa index,  $\alpha = 2.3$  in the linear form of Kroupa IMF (Kroupa 2001). For example, the mass distribution plot for IRAS 06063+2040 is shown in Fig. 4, which is fitted with a power-law of best-fit index,  $\Gamma \sim 1.22 \pm 0.16$ . Since the best-fitted IMF slopes are within the uncertainty of the Kroupa slope, so, we used the Kroupa broken power-law to calculate the total stellar mass of all the clusters. Briefly, we first integrated the IMFs of the clusters with the Kroupa index for mass limits of 0.5 to  $15 M_{\odot}$  and then extrapolated it down to  $0.1 M_{\odot}$  using the functional form of the Kroupa mass function. Doing so, we obtained the stellar masses of the clusters in the range between 43 to  $500 M_{\odot}$  and these are listed in Table 4.

Using  $M_{\text{gas}}$ ,  $M_*$ , and  $t_{\text{clust}}$ , we estimated the instantaneous SFR and SFE of the clusters. We find that the SFEs of the clusters lie in the range of 0.07 to 0.51, with a mean and median around 0.23 and

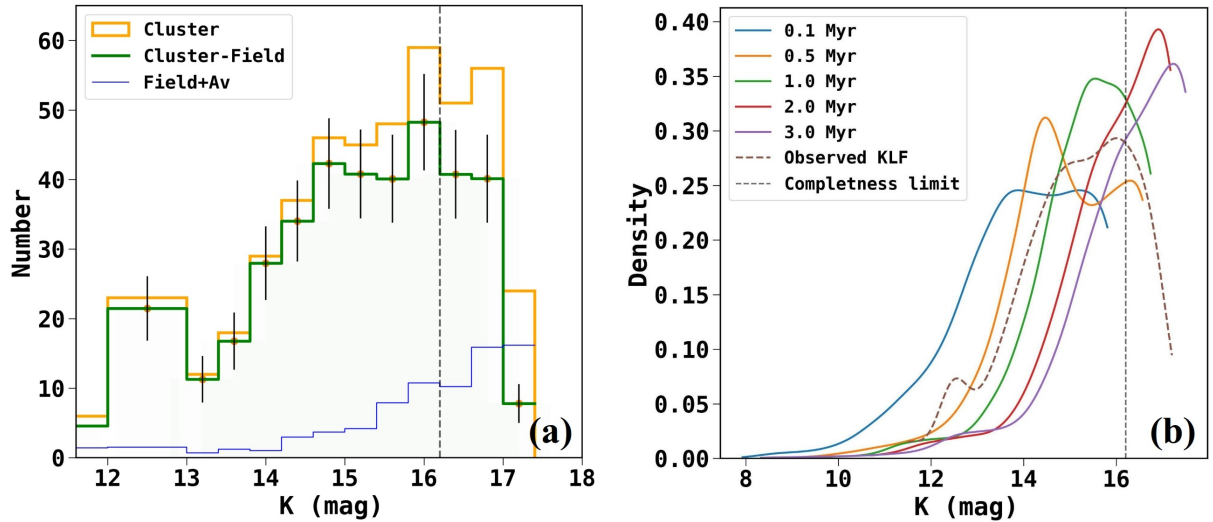


**Figure 3.** (a)  $K$ -band luminosity function of the IRAS 06063+2040 cluster (orange), reddened control field (blue), and control field subtracted cluster (green). (b)  $K$ -band density plots of synthetic clusters of age 0.1, 0.5, 1.0, 2.0, and 3.0 Myr, shown by solid curves. The dashed curve shows the control field subtracted  $K$ -band density plot of IRAS 06063+2040. The dashed grey line shows the completeness limit of the  $K$ -band data within the cluster region.

**Table 3.** Clump physical properties.

No	Name	$R_{\text{clust}}$ (pc)	$A_V$ (mag)	$t_{\text{clust}}$ (Myr)	$M_{\text{gas}}$ ( $M_{\odot}$ )	$\Sigma_{\text{gas}}$ ( $M_{\odot} \text{ pc}^{-2}$ )	$n_{\text{H}_2}$ ( $\text{cm}^{-3}$ )	$t_{\text{ff}}$ (Myr)
1	IRAS 06063+2040	$0.97 \pm 0.19$	6.0	$0.750 \pm 0.375$	$460 \pm 253$	$155 \pm 105$	$1732 \pm 1403$	$0.74 \pm 0.30$
2	IRAS 06055+2039	$0.79 \pm 0.16$	8.6	$0.750 \pm 0.375$	$810 \pm 446$	$410 \pm 279$	$5628 \pm 4559$	$0.41 \pm 0.17$
3	IRAS 06068+2030	$0.87 \pm 0.17$	5.1	$0.50 \pm 0.25$	$300 \pm 165$	$126 \pm 86$	$1564 \pm 1267$	$0.78 \pm 0.32$
4	IRAS 22134+5834	$0.48 \pm 0.10$	7.5	$1.50 \pm 0.75$	$120 \pm 66$	$167 \pm 114$	$3796 \pm 3075$	$0.50 \pm 0.20$
5	IRAS 06056+2131	$0.51 \pm 0.10$	8.5	$0.50 \pm 0.25$	$400 \pm 220$	$485 \pm 330$	$10263 \pm 8313$	$0.30 \pm 0.12$
6	Sh2-255 IR	$1.00 \pm 0.06$	10	$1.0 \pm 0.5$	$1400 \pm 560$	$398 \pm 167$	$4151 \pm 1826$	$0.48 \pm 0.11$
7	[IBP2002] CC14	$0.57 \pm 0.11$	6.6	$0.750 \pm 0.375$	$210 \pm 116$	$206 \pm 140$	$3914 \pm 3170$	$0.49 \pm 0.20$
8	IRAS 06058+2138	$0.62 \pm 0.12$	10.1	$0.750 \pm 0.375$	$580 \pm 319$	$487 \pm 331$	$8606 \pm 6971$	$0.33 \pm 0.13$
9	IRAS 06065+2124	$0.64 \pm 0.13$	5.0	$1.50 \pm 0.75$	$150 \pm 82$	$113 \pm 77$	$1908 \pm 1546$	$0.70 \pm 0.29$
10	NGC 2282	$0.84 \pm 0.20$	2.3	$2.0 \pm 1.0$	$170 \pm 102$	$77 \pm 58$	$996 \pm 922$	$0.98 \pm 0.49$
11	IRAS 05490+2658	$1.02 \pm 0.20$	10.7	$0.50 \pm 0.25$	$930 \pm 512$	$284 \pm 193$	$3036 \pm 2459$	$0.56 \pm 0.23$
12	BFS 56	$0.90 \pm 0.18$	8.4	$1.0 \pm 0.5$	$520 \pm 286$	$215 \pm 146$	$2670 \pm 2163$	$0.60 \pm 0.24$
13	Sh2-88	$0.54 \pm 0.02$	8.5	$0.30 \pm 0.15$	$590 \pm 230$	$653 \pm 261$	$13266 \pm 5413$	$0.27 \pm 0.05$
14	IRAS 06103+1523	$0.46 \pm 0.09$	9.1	$1.250 \pm 0.625$	$450 \pm 248$	$676 \pm 460$	$30778 \pm 24930$	$0.24 \pm 0.10$
15	IRAS 06104+1524A	$0.46 \pm 0.09$	7.3	$1.0 \pm 0.5$	$170 \pm 94$	$258 \pm 175$	$6095 \pm 4937$	$0.39 \pm 0.16$
16	IRAS 06117+1901	$1.60 \pm 0.32$	3.1	$1.50 \pm 0.75$	$640 \pm 352$	$80 \pm 54$	$545 \pm 441$	$1.32 \pm 0.51$
17	IRAS 05480+2545	$0.80 \pm 0.16$	6.4	$0.750 \pm 0.375$	$1100 \pm 605$	$551 \pm 375$	$7432 \pm 6020$	$0.36 \pm 0.14$

0.20, respectively. The SFRs lie in the range 29 to  $500 M_{\odot} \text{ Myr}^{-1}$ , with a mean and median around  $184 M_{\odot} \text{ Myr}^{-1}$  and  $163 M_{\odot} \text{ Myr}^{-1}$ , respectively. The spread in the SFEs may occur due to the different evolutionary stages of the clusters (e.g. Dib et al. 2011; Lee et al. 2016). The SFE of a region initially rises with time as a result of star formation and later can increase due to the decrease in the cluster's gas mass caused by the conversion of gas into stars and/or the dispersal of gas from feedback mechanisms. The latter effect could bias the instantaneous SFE due to the way it is defined. Therefore, the instantaneous SFE is only reliable for young star-forming regions, which are at the early stages and have significant gas mass left to form stars. In our case, most of the clusters are very young and associated with gas of high surface density (gas with corresponding  $A_V > 7-8$  mag or  $\Sigma_{\text{gas}} = 110-130 M_{\odot} \text{ pc}^{-2}$ , see Table 3). In molecular clouds, structures with  $A_V > 7-8$  mag are, in general, found to be the preferred sites of active star formation (Lada et al. 2010; André 2017;

Patra et al. 2022). Moreover, we find that stellar feedback is not yet significant in these clumps to significantly affect star formation properties (discussed in Section 4.2). Therefore, in our case, the estimated SFE and SFR are likely free from the biases discussed above. The efficiency can also be expressed as the fraction of gas mass converted into stars per free-fall time, which is defined as  $\epsilon_{\text{ff}} = \text{SFE} \times t_{\text{ff}} / t_{\text{clust}}$ . The  $\epsilon_{\text{ff}}$  of the clusters ranges from 0.03 to 0.34, with a mean and median around 0.15 and 0.13, respectively. The variation of SFE and  $\epsilon_{\text{ff}}$  of the clusters is shown in Fig. 5 with their  $\Sigma_{\text{gas}}$ . Sh2-255 IR cluster has the maximum SFR (i.e.  $\sim 500 M_{\odot} \text{ Myr}^{-1}$ ), while IRAS 06065+2124 has the minimum SFR (i.e.  $\sim 29 M_{\odot} \text{ Myr}^{-1}$ ). However, we want to emphasize that the measured SFE and SFR are instantaneous observational values. If the clumps are part of dynamically evolving clouds, these instantaneous values are likely biased toward high SFEs and SFRs, as the extended reservoir that could supply additional material to the clump is not accounted for. The measured

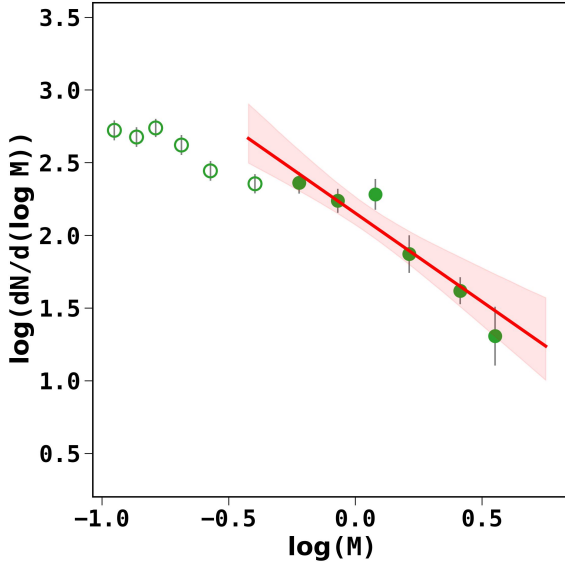


**Figure 4.** The cluster mass distribution function of IRAS 06063+2040 in which the error bars represent the  $\pm\sqrt{N}$  errors. The filled circles show the data points used for the least square fit with a power-law function, and the best-fit index,  $\Gamma$ , is  $\sim 1.22 \pm 0.16$ . The shaded region shows the  $3\sigma$  uncertainty associated with the fitted index.

star formation properties are given in Table 3 and 4 and the uncertainties in the estimated parameters are derived by propagating errors associated with the gas mass, stellar mass, distance, and age of the clumps.

### 3.6 Scaling relations at clump scale

Observational studies show that the number of young stars is correlated with the gas density, which means that most of the YSOs form in the higher-density structures of the cloud (Heiderman et al. 2010; Lada et al. 2012; Lada et al. 2013; Evans et al. 2014). Therefore, to investigate the relation between the SFR and gas mass, we determined  $\Sigma_{\text{SFR}}$  and  $\Sigma_{\text{gas}}$  by dividing the SFR and gas mass from the projected area ( $A_{\text{clust}} = \pi R_{\text{clust}}^2$ ) of the clumps on the plane of the sky. The  $\Sigma_{\text{SFR}}$  and  $\Sigma_{\text{gas}}$  values for all the clusters are given in Table 4. The mean and median  $\Sigma_{\text{SFR}}$  of the clusters in our sample are  $\sim 114$  and  $\sim 101 M_{\odot} \text{ Myr}^{-1} \text{ pc}^{-2}$ , respectively, while the mean and median  $\Sigma_{\text{gas}}$  are  $\sim 314$  and  $\sim 258 M_{\odot} \text{ pc}^{-2}$ , respectively. Fig. 6 illustrates the variation of  $\Sigma_{\text{SFR}}$  with  $\Sigma_{\text{gas}}$ , which shows a positive correlation. The Pearson correlation coefficient in the log-log scale is around 0.73. As discussed earlier, scaling relations follow a power-law relation ( $\Sigma_{\text{SFR}} = A \Sigma_{\text{gas}}^N$ ), which in the logarithmic form can be expressed as

$$\log\left(\frac{\Sigma_{\text{SFR}}}{1M_{\odot} \text{ Myr}^{-1} \text{ pc}^{-2}}\right) = \log A + N \log\left(\frac{\Sigma_{\text{gas}}}{1M_{\odot} \text{ pc}^{-2}}\right). \quad (11)$$

To consider the errors in both axes, we adopted the Orthogonal Distance Regression (ODR) method (Boggs et al. 1988) to fit the data points. With ODR, the best-fit  $N$  turns out to be  $\sim 1.46 \pm 0.28$ . In Fig. 6, we also show the position of the young cluster FSR 655, studied by Rawat et al. (2024a) using a method similar to the one employed in this work.

The theoretical models (Krumholz & McKee 2005; Krumholz

No	Name	$M_*$ ( $M_{\odot}$ )	SFE	SFR ( $M_{\odot} \text{ Myr}^{-1}$ )	$\Sigma_{\text{SFR}}$ ( $M_{\odot} \text{ Myr}^{-1} \text{ pc}^{-2}$ )	$\Sigma_{\text{gas}}/f_{\text{ff}}$ ( $M_{\odot} \text{ Myr}^{-1} \text{ pc}^{-2}$ )	$S_{\nu}$ (mJy)	$\log\left(\frac{N_{\text{bc}}}{\text{s}^{-1}}\right)$	$\frac{F_{\text{grav}}}{F_{\text{rad}}}$
1	IRAS 06063+2040	$223 \pm 24$	$0.33 \pm 0.12$	$297 \pm 152$	$101 \pm 65$	$210 \pm 166$	$41.09 \pm 0.69$	$46.191 \pm 0.009$	5.5
2	IRAS 06055+2039	$201 \pm 22$	$0.20 \pm 0.09$	$268 \pm 137$	$137 \pm 89$	$1000 \pm 791$	$119.76 \pm 0.35$	$46.656 \pm 0.006$	16.2
3	IRAS 06068+2030	$83 \pm 7$	$0.22 \pm 0.09$	$166 \pm 84$	$70 \pm 45$	$162 \pm 128$	$76.37 \pm 0.33$	$46.460 \pm 0.006$	2.2
4	IRAS 22134+5834	$125 \pm 10$	$0.51 \pm 0.14$	$83 \pm 42$	$115 \pm 76$	$334 \pm 264$	$3.24 \pm 0.20$	$44.794 \pm 0.027$	5.4
5	IRAS 06056+2131	$91 \pm 7$	$0.19 \pm 0.08$	$182 \pm 92$	$223 \pm 143$	$1596 \pm 1263$	$2.71 \pm 0.76$	$44.909 \pm 0.122$	48.5
6	Sh2-255 IR	$500 \pm 50$	$0.26 \pm 0.08$	$500 \pm 255$	$159 \pm 83$	$833 \pm 395$	$34.1 \pm 3.5$	$46.048 \pm 0.045$	55.0
7	[IBP2002] CC14	$47 \pm 5$	$0.18 \pm 0.08$	$63 \pm 32$	$61 \pm 40$	$419 \pm 331$	$0.024 \pm 0.002$	$42.822 \pm 0.044$	55.1
8	IRAS 06058+2138	$127 \pm 16$	$0.18 \pm 0.08$	$169 \pm 87$	$140 \pm 90$	$1476 \pm 1161$	$1.10 \pm 0.11$	$44.519 \pm 0.044$	96.1
9	IRAS 06065+2124	$43 \pm 4$	$0.22 \pm 0.10$	$29 \pm 15$	$22 \pm 15$	$160 \pm 127$	$0.014 \pm 0.001$	$42.679 \pm 0.044$	24.7
10	NGC 2282	$89 \pm 13$	$0.34 \pm 0.14$	$45 \pm 23$	$20 \pm 14$	$79 \pm 70$	$10.30 \pm 2.20$	$45.405 \pm 0.093$	2.1
11	IRAS 05490+2658	$220 \pm 23$	$0.19 \pm 0.09$	$440 \pm 225$	$135 \pm 87$	$508 \pm 402$	$1.962 \pm 0.838$	$44.889 \pm 0.186$	66.8
12	BFS 56	$70 \pm 7$	$0.12 \pm 0.06$	$70 \pm 36$	$28 \pm 18$	$361 \pm 285$	$0.036 \pm 0.004$	$43.156 \pm 0.044$	106.4
13	Sh2-88	$122 \pm 11$	$0.17 \pm 0.06$	$407 \pm 207$	$444 \pm 228$	$2442 \pm 1096$	$4189.0 \pm 59.0$	$48.160 \pm 0.006$	3.6
14	IRAS 06103+1523	$72 \pm 8$	$0.14 \pm 0.07$	$58 \pm 30$	$87 \pm 56$	$2750 \pm 2176$	$1.0 \pm 0.1$	$44.588 \pm 0.044$	99.2
15	IRAS 06104+1524A	$83 \pm 9$	$0.33 \pm 0.12$	$83 \pm 43$	$125 \pm 80$	$654 \pm 518$	$5.73 \pm 0.75$	$45.291 \pm 0.057$	7.7
16	IRAS 06117+1901	$245 \pm 26$	$0.28 \pm 0.11$	$163 \pm 84$	$20 \pm 13$	$61 \pm 48$	$14.34 \pm 1.43$	$45.772 \pm 0.044$	5.8
17	IRAS 05480+2545	$81 \pm 9$	$0.07 \pm 0.04$	$108 \pm 55$	$54 \pm 35$	$1543 \pm 1221$	$0.54 \pm 0.05$	$44.363 \pm 0.044$	236.1

**Table 4.** Cluster properties.

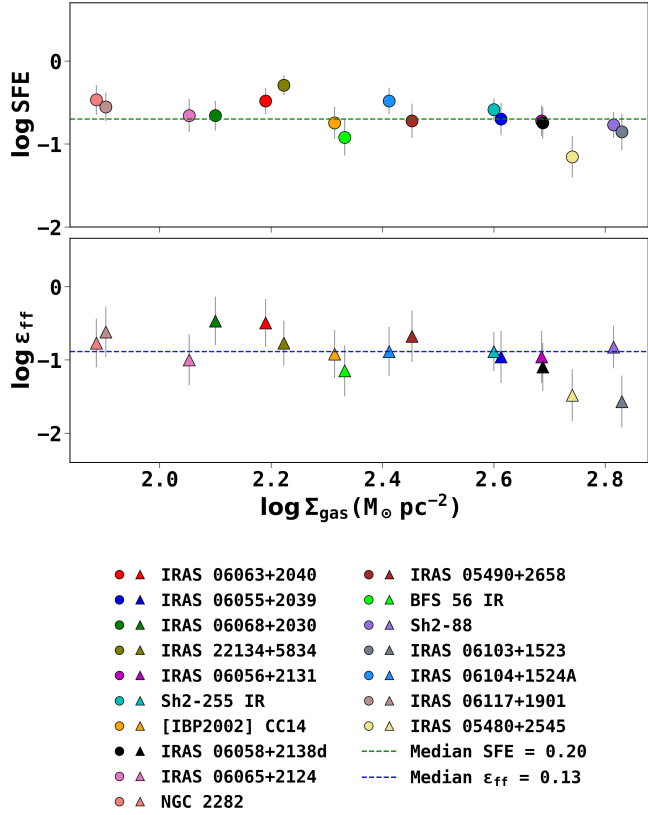


**Figure 5.** The SFE and  $\epsilon_{\text{ff}}$  of the clusters plotted with their gas mass surface densities.

et al. 2019) predict the dependence of star formation rate on the free-fall time of the clouds. It has also been found observationally that the inclusion of the free-fall time reduces the scatter in the SFR–gas mass relation (Krumholz et al. 2012; Pokhrel et al. 2021). This relation is the volumetric star formation relation, which in logarithmic form can be expressed as

$$\log \left( \frac{\Sigma_{\text{SFR}}}{1 M_{\odot} \text{Myr}^{-1} \text{pc}^{-2}} \right) = \log A' + N' \log \left( \frac{\Sigma_{\text{gas}}/t_{\text{ff}}}{1 M_{\odot} \text{Myr}^{-1} \text{pc}^{-2}} \right), \quad (12)$$

where  $t_{\text{ff}}$  depends only on the volume density of the region. For the studied sample, we found that the  $\Sigma_{\text{gas}}/t_{\text{ff}}$  lies in the range of  $\sim 61$  to  $2750 M_{\odot} \text{Myr}^{-1} \text{pc}^{-2}$  with a mean and median around  $858 M_{\odot} \text{Myr}^{-1} \text{pc}^{-2}$  and  $508 M_{\odot} \text{Myr}^{-1} \text{pc}^{-2}$ , respectively. Fig. 7 shows the  $\Sigma_{\text{SFR}}$  vs  $\Sigma_{\text{gas}}/t_{\text{ff}}$  plot, which are well correlated with a Pearson’s coefficient of  $\sim 0.74$ . We fitted the relation with equation 12 using the ODR method and found the best-fit value of  $N'$  as  $\sim 0.80 \pm 0.15$ . The exponent value obtained for clumps matches well, within the uncertainty, with the mean and median exponent values reported by Pokhrel et al. (2021) (i.e.  $\sim 0.94$  and  $\sim 0.99$ , respectively) for volumetric star formation relation at the cloud scale.

## 4 DISCUSSION

### 4.1 Comparison with existing star formation scaling relations

As already discussed, several previous studies investigated the scaling relations at cloud scale or within single clouds (Evans et al. 2009; Lada et al. 2010; Heiderman et al. 2010; Gutermuth et al. 2011; Krumholz et al. 2012; Evans et al. 2014; Hony et al. 2015; Vutisalchavakul et al. 2016; Das et al. 2021; Pokhrel et al. 2021). It is important to acknowledge that the shapes of the scaling relations are sensitive to the adopted methodologies (see Table 1) due to systematic uncertainties and data quality. Therefore, we do not intend to directly compare the derived scaling relations with those from previous studies but instead want to analyze them in the context of the trends observed in the aforementioned studies. These studies have been done over the nearby clouds ( $< 1$  kpc) and are based on the star count method to determine the SFR. The aforementioned studies tested scaling relations in various forms and found different power-law exponents, which, up to some extent, can be attributed to the differences in methodology, like data resolution, SFR tracers, fitting methods, gas tracers, and completeness of the YSO sample. Moreover, some of the studies found that there is relatively large scatter and loose correlation in the SFR–gas mass relation between clouds in comparison to within single clouds (e.g. Lada et al. 2013; Evans et al. 2014).

In Fig. 8, a comparison of the results of this work with the existing scaling relations at the extragalactic and cloud/clump scale are shown. From the figure, it can be seen that although the value of the exponent obtained in this work ( $\sim 1.5$ ) is similar to the KS power law index ( $\sim 1.4$ ; Kennicutt 1998b), the data points from our sample of clumps lie well above the KS relation. Fig. 8 also shows the linear relation between  $\Sigma_{\text{SFR}}$  and molecular gas surface density obtained by Bigiel et al. (2008) for 18 nearby galaxies at  $\sim 750$  pc scales, with  $\Sigma_{\text{H}_2}$  in the range of  $3$ – $50 M_{\odot} \text{pc}^{-2}$ . The data points of this work also show much higher  $\Sigma_{\text{SFR}}$  values than predicted by the linear relation of Bigiel et al. (2008). The higher trend of scaling relations than the extragalactic ones has also been found at the cloud scale by other observational studies (Evans et al. 2009; Lada et al. 2010; Heiderman et al. 2010; Hony et al. 2015). From the figure, one can also see that our studied sample shows higher values in comparison to nearby clouds from c2d and GB survey (Evans et al. 2009; Lada et al. 2010; Heiderman et al. 2010; Evans et al. 2014). Heiderman et al. (2010) also examined the scaling relation for the youngest YSOs (e.g. Class I) and found that their  $\Sigma_{\text{SFR}}$  is higher than the values obtained by including all the YSOs in the clouds, which is also shown in Fig. 8. From the figure, it can also be seen that though the Class I YSO sample of Heiderman et al. (2010) is closest to our sample, still the clumps within our sample exhibit higher values of  $\Sigma_{\text{SFR}}$  compared to their Class I YSO sample. As discussed earlier, the GB survey traces low-mass star-forming clouds, which may influence the derived values of the SFRs and SFEs. Pokhrel et al. (2021) studied 12 nearby MCs and obtained the  $\Sigma_{\text{SFR}} - \Sigma_{\text{gas}}$  relation within individual clouds, with a mean and median power-law exponent of  $\sim 2.00$  and  $\sim 2.08$ , respectively, and a cloud-to-cloud spread of  $\sim 0.3$  dex in  $\Sigma_{\text{SFR}}$  at logarithmic scale. The obtained power law exponent in this work is shallower, but still consistent within  $2\sigma$  uncertainty. However, as can be seen from Fig. 8, our cluster sample lies above the Pokhrel et al. (2021) scaling relation. As discussed in Suin et al. (2024), the sensitivity and resolution of the data influence the determination of the star formation properties and, consequently, the scaling relations. This is particularly true in the cluster environment, where the bright background affects the detection of the faint point sources in the

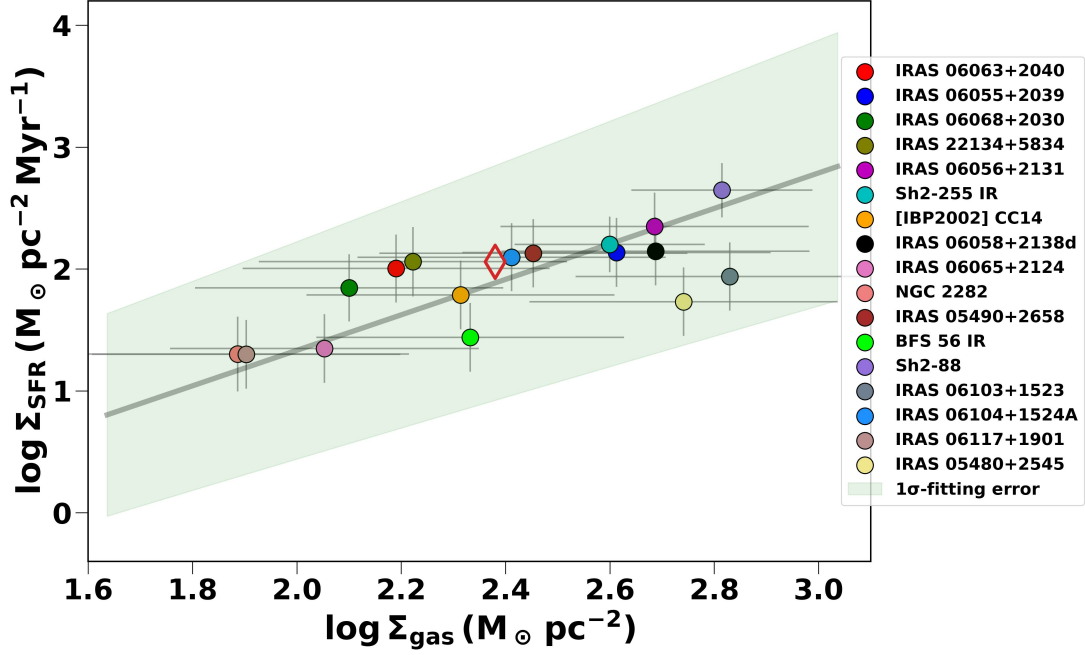


**Figure 6.** Variation of  $\log \Sigma_{\text{SFR}}$  with  $\log \Sigma_{\text{gas}}$ . The black line shows the ODR fit with a best-fit power law exponent of  $\sim 1.5$  along with  $1\sigma$  uncertainty shown as a green shaded region. The diamond symbol denotes the FSR 655 cluster studied in [Rawat et al. \(2024a\)](#).

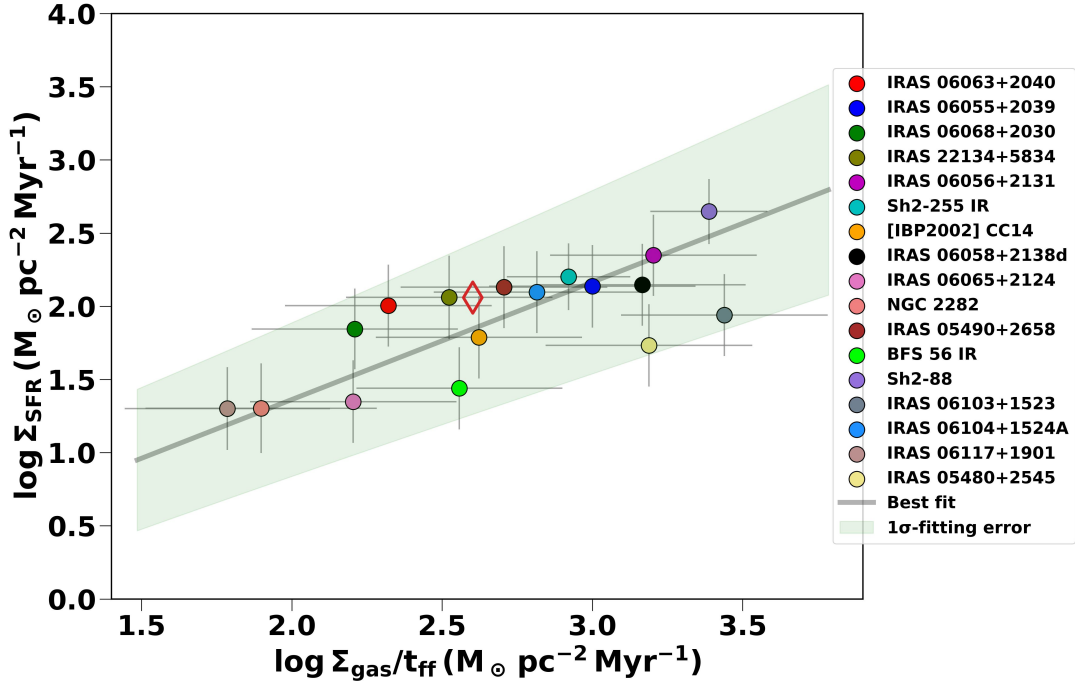


**Figure 7.** Variation of  $\log \Sigma_{\text{SFR}}$  with  $\log \Sigma_{\text{gas}}/t_{\text{ff}}$ . The black line shows the ODR fit with a best-fit power law exponent of  $\sim 0.8$  along with  $1\sigma$  uncertainty shown as a green shaded region. The diamond symbol is the same as in Fig. 6.

*Spitzer* bands compared to NIR bands (e.g. see Figure 13 of [Rawat et al. 2024a](#)).

At the clump scale, [Heiderman et al. \(2010\)](#) investigated the SFR–gas mass relation in massive dense clumps (mean radius  $\sim 1.13$  pc) from [Wu et al. \(2010\)](#) that are traced by HCN (1–0) molecular line data. The authors calculated the gas mass from HCN and SFR

from infrared luminosities (8–1000  $\mu\text{m}$ ) and obtained a linear dependence of  $\Sigma_{\text{SFR}}$  on  $\Sigma_{\text{HCN}}$ , which is also shown in Fig. 8. From the figure, it can be seen that our cluster sample lies above their relation. In this case, more than half of the sample of [Wu et al. \(2010\)](#) consists of clumps beyond 4 kpc. At large distances, some faint low-mass stars might be missed, leading to an underestimation of the SFR. The

massive clumps from the study of [Heyer et al. \(2016\)](#) are also shown in the figure, and it can be seen that few of them lie close to our cluster sample. [Heyer et al. \(2016\)](#) studied star formation scaling relations in massive clumps of the Milky Way by selecting the clumps from APEX Telescope Large Area Survey of the Galaxy (ATLASGAL; [Schuller et al. 2009](#)) data and linking them to the YSOs from the catalogue of *Spitzer* 24  $\mu\text{m}$  MIPS GAL survey. The authors calculated the total gas mass from the 870  $\mu\text{m}$  flux and evaluated the total stellar mass by sampling the IMF and computed the SFR by dividing the inferred stellar mass by time scales of 0.5 Myr. Our sample shows higher values in comparison to clumps studied by [Heyer et al. \(2016\)](#). A possible explanation is that due to the lower sensitivity of the MIPS GAL 24  $\mu\text{m}$  data, the mass sensitivity limit of the [Heyer et al. \(2016\)](#)'s YSO sample is only down to  $2 M_{\odot}$ . In most of the clumps, they detected only one or a few protostars in 24  $\mu\text{m}$ , which might have added uncertainty in estimating the total stellar mass of the clumps in their study. In addition, [Heyer et al. \(2016\)](#)'s clumps are likely at earlier evolutionary stages compared to the clumps studied in this work. We want to emphasize that, although the NIR data used in this work are largely complete down to  $0.2 M_{\odot}$ , however, we have accounted for all the stars down to  $0.1 M_{\odot}$  by extrapolating the IMF while estimating the clusters' properties.

Fig. 9 shows the comparison of the volumetric star formation relation obtained for cluster sample in this work with those observed in some of the previous studies at the cloud scale. Similar to the  $\Sigma_{\text{SFR}} - \Sigma_{\text{gas}}$  plot, it is clearly evident from the  $\Sigma_{\text{SFR}} - \Sigma_{\text{gas}}/t_{\text{ff}}$  plot that our cluster sample lies above the nearby clouds of previous studies ([Heiderman et al. 2010](#); [Lada et al. 2010](#); [Evans et al. 2014](#); [Pokhrel et al. 2021](#)). The obtained slope of the volumetric star formation relation for the cluster sample of this work is almost the same as found in [Pokhrel et al. \(2021\)](#) (i.e. 0.94); however, it is apparent from the figure that the trend line for our cluster sample lies above that of [Pokhrel et al. \(2021\)](#)'s relation. [Krumholz & McKee \(2005\)](#) theoretically derived the value of  $\epsilon_{\text{ff}}$  to be  $\approx 0.01$  for any supersonically turbulent medium. At large scales (length  $\sim 100$  pc) also, the  $\epsilon_{\text{ff}}$  is found to be  $\approx 0.01$  in nearby galaxies using CO molecular data and IR luminosities (see [Chevance et al. 2023](#), and references therein). For Galactic MCs, nearby galaxies, and high redshift galaxies, [Krumholz et al. \(2012\)](#) also observed a linear relation between  $\Sigma_{\text{SFR}}$  and  $\Sigma_{\text{gas}}/t_{\text{ff}}$  along with a  $\epsilon_{\text{ff}}$  value of  $\sim 0.01$ , which they suggested would be roughly constant with a dispersion of  $\sim 0.3$  dex (see also Figure 10 of [Krumholz et al. 2019](#)). The study by [Pokhrel et al. \(2021\)](#) in nearby clouds, found  $\epsilon_{\text{ff}}$  in the range of 0.010 to 0.043, with a median around 0.026, and did not find any threshold density above which the  $\epsilon_{\text{ff}}$  rises significantly. Fig. 9 shows that although the best-fit slope ( $\sim 0.8$ ) found here fairly matches the linear relation of [Krumholz et al. \(2012\)](#) (shown by a solid black line) within the uncertainty, the  $\epsilon_{\text{ff}}$  for our cluster sample is higher than their obtained value of 0.01. While the mean  $\epsilon_{\text{ff}}$  value for our cluster sample is  $\sim 0.15$ , fixing the slope of  $\Sigma_{\text{SFR}} - \Sigma_{\text{gas}}/t_{\text{ff}}$  relation to unity (i.e.  $\Sigma_{\text{SFR}} \propto \Sigma_{\text{gas}}/t_{\text{ff}}^{1.0}$ ), the best-fit  $\epsilon_{\text{ff}}$  value from the ODR regression fit comes around 0.16 (shown by a dashed black line in Fig. 9), which is 16 times higher than the theoretical  $\epsilon_{\text{ff}}$  value of  $\sim 0.01$  ([Krumholz & McKee 2005](#)).

Although the power law exponent in  $\Sigma_{\text{SFR}} - \Sigma_{\text{gas}}$  relation for our cluster sample is somewhat comparable with the previous studies within the uncertainty, the surface density values of the SFR at the same gas mass surface densities are relatively higher. These high values of  $\Sigma_{\text{SFR}}$  for our cluster sample can be explained by the following reasons: (i) the regions studied in this work are relatively much smaller than those at extragalactic scales ([Kennicutt 1998b](#); [Bigiel et al. 2008](#)), (ii) our sample consists of cluster forming regions, i.e. ac-

tive star-forming regions; however, at cloud and mainly extragalactic scales, averaging over large regions includes both active and quiescent (i.e. diffused non-star forming gas) star-forming regions. As a consequence, regions in our sample have higher SFRs within smaller plane-of-sky projected surface areas, hence larger  $\Sigma_{\text{SFR}}$  values. A less scatter in the SFR–gas mass relation found here (see Fig. 8 and 9) can be explained by the adopted methodology for calculating the total stellar mass and the narrow evolutionary spread of the clumps, i.e. the ages of most of the embedded clusters are in the range 0.5–1.5 Myr. In this work, to get the total stellar mass, we extrapolated the IMF down to the low mass limit of  $\sim 0.1 M_{\odot}$  and calculated the ages of the clusters as a whole by comparing them with the synthetic clusters of different ages. While, in some of the previous studies, a single average mass ( $\sim 0.5 M_{\odot}$ ) and age ( $\sim 2$  Myr) for all YSOs were adopted ([Evans et al. 2009](#); [Lada et al. 2010](#); [Heiderman et al. 2010](#); [Evans et al. 2014](#)). To avoid the uncertainty caused by including the Class II YSOs, some of the previous studies included only young protostars (e.g. Class I) and found relatively better correlation between  $\Sigma_{\text{SFR}}$  and  $\Sigma_{\text{gas}}$  ([Heiderman et al. 2010](#); [Lombardi et al. 2013](#); [Lada et al. 2013](#); [Evans et al. 2014](#); [Willis et al. 2015](#)).

Apart from the above facts, in our cluster sample, except for NGC 2282 and IRAS 06117+1901, all other clusters have gas mass surface densities greater than  $110 M_{\odot} \text{pc}^{-2}$ . A density threshold of  $\sim 110\text{--}130 M_{\odot} \text{pc}^{-2}$  (or  $7\text{--}8 A_V$ ) has been suggested in the literature above which the SFR varies linearly with the mass of dense gas and is better correlated ([Lada et al. 2010](#); [Heiderman et al. 2010](#); [Evans et al. 2014](#); [Das et al. 2021](#); [Patra et al. 2022](#)). In fact, 14 out of 17 clusters in our sample have gas mass surface densities  $\geq 130 M_{\odot} \text{pc}^{-2}$ , which could also be a reason for a better correlation of the SFR with gas mass in the present work. Simulations also suggest a better correlation between SFR and gas mass at higher threshold density as a consequence of larger gravitational influence ([Burkhart et al. 2013](#); [Sokolov et al. 2019](#)).

Fig. 10 shows the plot of average SFEs with the gas mass surface densities of clouds, clumps, and cores. The mean SFE at the cloud scale is taken from the studies of nearby clouds ([Evans et al. 2009](#); [Heiderman et al. 2010](#); [Lada et al. 2010](#); [Evans et al. 2014](#)), which are based on the star count method. From these studies, the SFE at the molecular cloud scale turns out to be around  $2.6 \pm 2.0\%$ . At the clump scale, the median SFE is around  $20 \pm 6.0\%$ , as obtained in this work from a sample of 17 cluster-forming clumps. At the core scale, the SFEs are indirectly derived from the similarity between the shape of the dense core mass function and the stellar IMF for a sample of nearby molecular clouds and massive star-forming regions ([Alves et al. 2007](#); [Könyves et al. 2010, 2015](#); [Di Francesco et al. 2020](#); [Zhou et al. 2024a](#)). These studies find that there is a one-to-one correlation between core and stellar masses, and the core-to-star formation efficiency is around  $30 \pm 10\%$ . Understanding how SFE evolves from cloud scale to core scale is of particular interest for the overall evolution of the molecular cloud. Our analysis reveals an increasing efficiency from cloud to core scales, consistent with the hierarchical cloud structure model, where efficiency increases with the average gas density from large-scale clouds down to dense cores ([Elmegreen 2008](#)). However, establishing a definitive relationship between different scales and SFE would require a diverse sample spanning a broad range of surface densities, spatial scales, and evolutionary stages of clouds.

#### 4.2 Possible reasons for high $\epsilon_{\text{ff}}$ at clump scale

In a recent work, [Zamora-Aviles et al. \(2024\)](#) simulated the collapse of a hub-filament system cloud under self-gravity to test the star

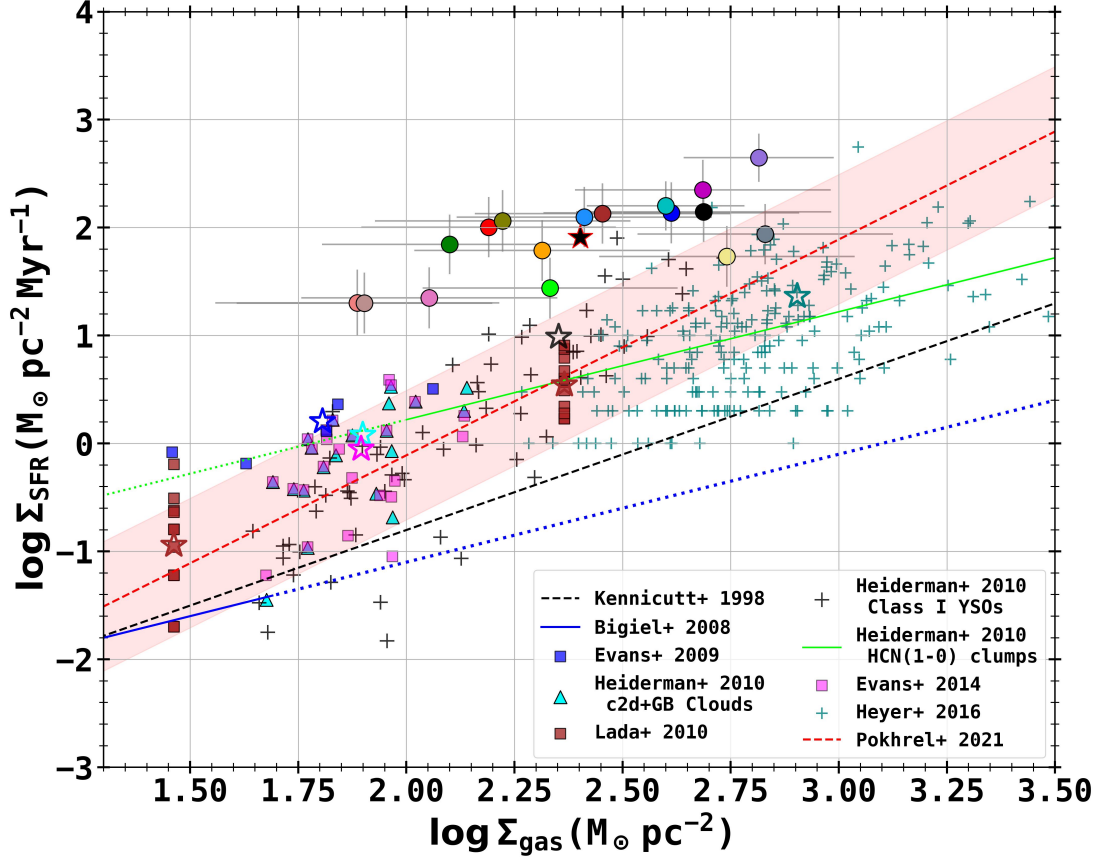


**Figure 8.** Comparison of the  $\Sigma_{\text{SFR}} - \Sigma_{\text{gas}}$  relation obtained in this work with existing relations in the literature. The solid colored dots denote the clusters in our sample, as shown in Fig. 6. The galactic-scale relations of Kennicutt (1998b) and Bigiel et al. (2008) are shown by black dashed and blue solid lines, respectively. The Bigiel et al. (2008)’s relation is extrapolated by a blue dotted line towards higher gas mass surface densities. The nearby clouds from Evans et al. (2009) (blue squares), Heiderman et al. (2010) (cyan triangles), Lada et al. (2010) (brown squares), and Evans et al. (2014) (pink squares) are shown. The black pluses show the  $\Sigma_{\text{SFR}} - \Sigma_{\text{gas}}$  values obtained for only Class I YSOs in the nearby clouds by Heiderman et al. (2010). The green solid line shows the relation obtained for HCN (1–0) massive dense clumps by Heiderman et al. (2010), which is extrapolated by a green dotted line towards lower gas mass surface densities. The teal pluses show the massive clumps from Heyer et al. (2016). The red dashed line shows the  $\Sigma_{\text{SFR}} - \Sigma_{\text{gas}}$  relation obtained by Pokhrel et al. (2021), with a spread shown as a red shaded area (see text for details). The mean  $\Sigma_{\text{SFR}} - \Sigma_{\text{gas}}$  in our sample is shown by a black solid star, and for other samples, the mean values are shown by open stars of the same colors as their corresponding sample.

formation-gas mass relations and found a similar exponent value for  $\Sigma_{\text{SFR}} - \Sigma_{\text{gas}}/t_{\text{ff}}$  relation (i.e.  $\sim 0.94$ ), as found in this work. Zamora-Aviles et al. (2024) suggest that the long lifetimes of clouds and their low SFE may not necessarily result from turbulent support against the cloud collapse, as proposed in gravo-turbulent model (Krumholz & McKee 2005, 2020), but could instead simply be a consequence of cloud collapse under gravity. The GHC (Vázquez-Semadeni et al. 2019) model suggests that the cloud appears to have a long lifetime because the accretion flows from low- to high-density regions continuously replenish the gas material in high-density regions to form stars. In this scenario, the SFR does not remain constant but increases over time till the stellar feedback becomes dominant to disrupt the cloud material, and then the SFR decreases (Vázquez-Semadeni et al. 2019). Zamora-Aviles et al. (2024) also suggest that the observationally obtained SFR–gas mass relations at cloud scales (Pokhrel et al. 2021), characterized by low and nearly constant values of  $\epsilon_{\text{ff}}$ , can be explained within the framework of the GHC model. The reasons behind low  $\epsilon_{\text{ff}}$  could be the accelerating SFR in clouds and the small free-fall time of high-density regions where stars are forming in comparison to the typical formation time of stars (for e.g.  $t = 2$  Myr for

up to Class II YSO stage) (for more details, see Zamora-Aviles et al. 2024). Due to these factors, the ratios on which the  $\epsilon_{\text{ff}}$  depends,  $t_{\text{ff}}/t$  and  $M_{\text{gas}}/M_{\text{gas}}^*$ , would become very small and hence the low  $\epsilon_{\text{ff}}$  values. The authors argue that due to the exponentially increasing SFR along with  $r^{-2}$  density profile, the total stellar mass formed from dense gas always remains smaller than the total gas mass of the whole region over which  $\epsilon_{\text{ff}}$  is calculated.

However, we note that in our study, cluster ages,  $t_{\text{clust}}$ , are determined as a whole using the KLFs. As a result, in most cases,  $t_{\text{clust}}$  is less than three times the  $t_{\text{ff}}$ , unlike the simulation results of Zamora-Aviles et al. (2024), where this ratio ranges from 12 to 17. Secondly, while it is true at the cloud scale that high-density star-forming gas comprises only a small fraction of the total cloud mass, the surface density of most clumps in our sample exceeds  $110 M_{\odot} \text{pc}^{-2}$ . Therefore, in this work, clump gas masses predominantly consist of dense gas, and as a result, the  $M_{\text{gas}}/M_{\text{gas}}^*$  ratio is not as low in our sample of clumps.

Like Zamora-Aviles et al. (2024), other studies also suggest that the photoionization feedback and stellar winds from the massive

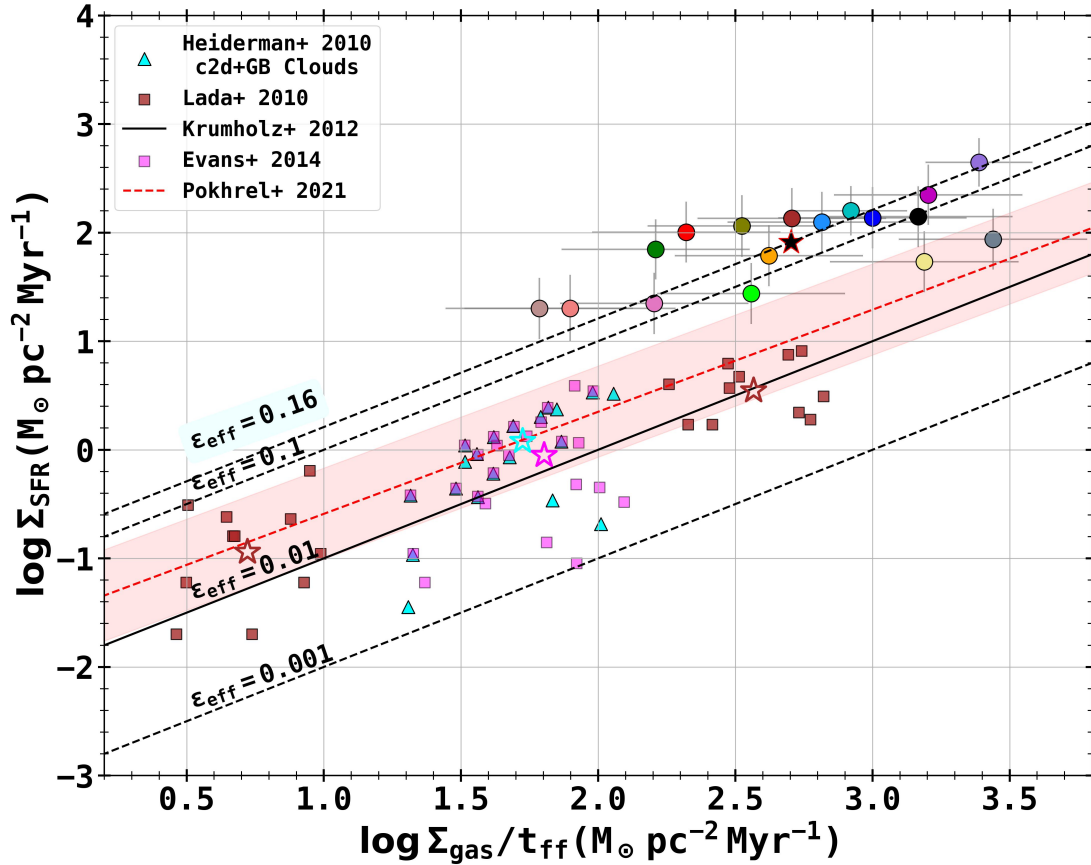


**Figure 9.** Comparison of  $\log \Sigma_{\text{SFR}}$  with  $\log \Sigma_{\text{gas}}/t_{\text{ff}}$ . The coloured symbols, red dashed line and red shaded region are the same as in Fig. 8. The black solid line shows the relation of *Krumholz et al. (2012)* and denotes the  $\epsilon_{\text{ff}}$  of 0.01, and the black dashed lines show the  $\epsilon_{\text{ff}}$  of 0.001, 0.1, and 0.16, respectively.

stars, in general, disperse the cloud material; thereby, significantly reduces the global star formation properties of a cloud (*Dib et al. 2011; Federrath & Klessen 2012; Dib et al. 2013; Dale et al. 2014; Geen et al. 2015; Krumholz et al. 2019*), although studies also suggest that feedback can also enhance star formation in some local regions of molecular clouds (*Zavagno et al. 2010; Chauhan et al. 2011; Deharveng et al. 2012; Samal et al. 2018*). In a recent simulation, *Suin et al. (2024)* show that  $\epsilon_{\text{ff}}$  varies with the gas mass surface density and the evolution of the star-forming region and is also influenced by the local environment, such as the presence of stellar feedback.

The presence of massive stars and their effect can be traced by measuring the thermal free-free radio continuum emission in a given region. Therefore, we obtained radio continuum images from the NRAO VLA Sky Survey (NVSS;  $\nu \sim 1.4$  GHz, beam  $\sim 45'' \times 45''$ ) and NRAO VLA Archive Survey (NVAS;  $\nu \sim 1.4$  GHz, beam  $\sim 45'' \times 45''$ ) (*Condon et al. 1998*) to search for radio emission in our cluster sample (e.g. shown in Fig. A1 for IRAS 06063+2040). For clumps that have negligible emission at 1.4 GHz, we search for images at  $\sim 5$  GHz in the VLA archive<sup>2</sup>, observed with the VLA D-configuration wherever applicable, considering the extended nature of the sources. For sources in which fluxes at both 1.4 GHz and 5 GHz are available, we prefer to use 5 GHz fluxes to minimize the effect of optical depth (e.g. *Yadav et al. 2022*) on the emission at these frequencies. We then calculated the integrated flux ( $S_{\nu}$ ) of the radio-emitting regions using

the Gaussian fitting tool in CASA. In our sample, we note that no radio emission was found for 5 sources at both 1.4 GHz and 5 GHz. In such cases, we estimated the integrated flux from the images within the cluster radius and considered these fluxes as the upper limit. The non-detection of radio emissions from a few sources implies that they may be at an early evolutionary stage of massive star formation. From the integrated flux, we estimated the Lyman continuum photons ( $N_{\text{Lyc}}$ ) associated with individual clusters, whose details are given in Appendix A. The  $S_{\nu}$  and  $N_{\text{Lyc}}$  values for the clusters are given in Table 4. The  $\log N_{\text{Lyc}}$  range of 42.7 to 48.2 suggests that the strength of feedback is different across our cluster sample.

As discussed above, the ionizing radiation from massive stars can affect the SFE of the clusters by halting the collapse or unbinding the gas present in the clump. Therefore, it is important to investigate the relative strength of radiation pressure ( $F_{\text{rad}}$ ) and gravitational pressure ( $F_{\text{grav}}$ ) in the clumps. So, we calculated  $F_{\text{rad}}$  and  $F_{\text{grav}}$  using the estimated  $N_{\text{Lyc}}$ , mass, and radius of the clumps, following the prescription given in *Murray (2009)* (for details, see Appendix A), and their ratios are given in Table 4. Fig. 11 shows the relative strength of both the forces in our sample, and as can be seen, the  $\frac{F_{\text{grav}}}{F_{\text{rad}}}$  is far greater than 2 for majority of the clusters in our sample, suggesting that although H II regions have developed in the 12 clumps, the clumps may still be collapsing and forming stars. As an example, we find that in the case of the Sh2-255 IR cluster in our sample, although NIR point sources and radio emissions have been observed by *Ojha et al. (2011)*, the region still hosts several compact

<sup>2</sup> <http://www.vla.nrao.edu/astro/nvas/>

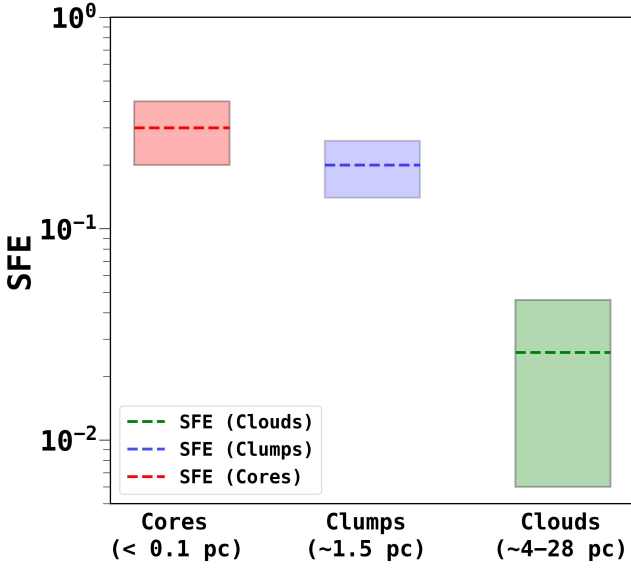


**Figure 10.** Star formation efficiencies at cloud, clump, and core scales. The red line shows the SFE of  $30 \pm 10\%$  at the core scale (Alves et al. 2007; Könyves et al. 2010, 2015; Di Francesco et al. 2020; Zhou et al. 2024a), the blue line shows the SFE of  $20 \pm 6\%$  at the clump scale found in this work, and the green line shows the SFE of  $2.6 \pm 2.0\%$  at the cloud scale (Evans et al. 2009; Heiderman et al. 2010; Lada et al. 2010; Evans et al. 2014). The corresponding colored shaded regions show the upper and lower limits of SFE at the respective scales. The mentioned range of cloud sizes is taken as the mean values from Table 1.

millimetre cores with no infrared point sources (Zinchenko et al. 2012, 2018), suggesting that stars are still forming in these clumps.

To understand the role of stellar feedback on the obtained scaling relations of the clumps, we normalized their gas mass surface densities by the associated number of Lyman continuum photons along with the free-fall time. Fig. 12 shows the variation of  $\Sigma_{\text{SFR}}$  with the  $\frac{\Sigma_{\text{gas}}}{t_{\text{ff}} N_{\text{Lyc}}}$  of the clusters. From the figure, it can be seen that  $\Sigma_{\text{SFR}}$  of the clusters remains flat with some evidence of a declining trend at high Lyman continuum photons. Our results hints to the fact that in young clusters like the ones studied in this work (i.e. regions of high gas surface densities), the stellar feedback does not seem to very significantly affect the star-formation properties. However, we acknowledge that given the small evolutionary range (i.e. 0.5–1.5 Myr for most of the sources) explored in this study and also the potential uncertainties associated with the age estimations, it is difficult to disentangle the effect of the evolutionary stages on the star formation properties of the studied sample. A better sample with a wider age range would be valuable in this regard. However, it is worth noting that, in a recent work, Zhou et al. (2024b) found that feedback does not seem to alter the dynamics of the gas in protocluster-forming regions significantly.

In summary, we believe that since our clumps are of compact size with high gas surface densities, currently actively forming stars, and the photoionization feedback effect is not yet significant, are the likely cause of high SFEs and SFRs compared to other studies. Deep NIR and mid-IR observations (e.g. with JWST) of younger clumps, like the ones explored by Heyer et al. (2016), would shed more light on the effects of temporal evolution on the scaling relations at the clump scale.

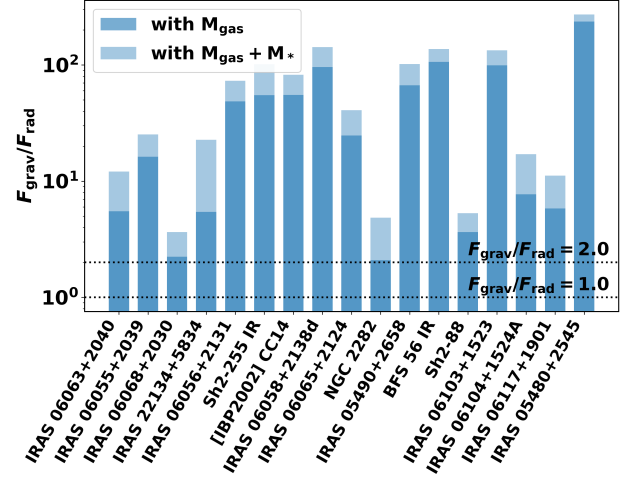


**Figure 11.** Ratio of gravitational to radiation pressure force for the clusters in our sample is shown. Dark blue bars represent values calculated using only the gas mass, while light blue bars include both gas and stellar mass in the calculation of  $F_{\text{grav}}$ .

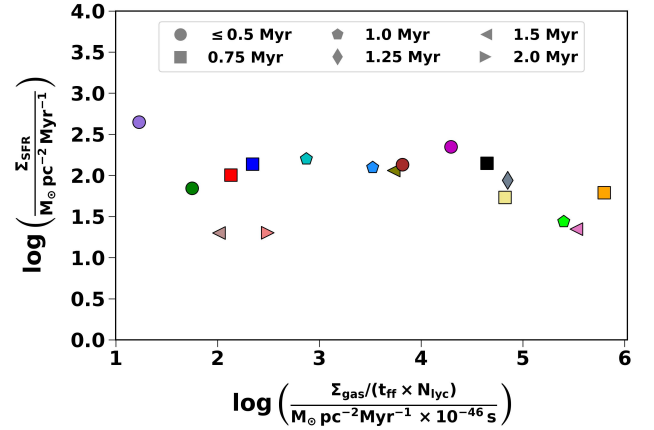


**Figure 12.** Comparison of  $\log \Sigma_{\text{SFR}}$  with  $\log \Sigma_{\text{gas}} / (t_{\text{ff}} \times N_{\text{Lyc}})$ . The colored symbols are the same as in Fig. 6.

### 4.3 Implication on bound cluster formation and infant mortality

As discussed in Section 1, it is believed that the formation of bound clusters strongly depends upon the efficiency by which the gas in MCs or clumps gets converted into stars. Many simulations showed that the bound fractions of newborn stars are tightly correlated with the SFEs (e.g. Shukirgaliyev et al. 2017; Li et al. 2019; Fukushima & Yajima 2021; Grudić et al. 2021). Therefore, the SFE is a key parameter for understanding the formation and early evolution of star clusters. Simulations suggest massive bound clusters ( $\geq 10^4 M_{\odot}$ ) formation through either a high mass gas assembly with a high SFE ( $\geq 30\%$ ) before the stellar feedback becomes significant (Dib et al. 2013; Longmore et al. 2014; Banerjee & Kroupa 2015; Krumholz et al. 2019), or gradual gas assembly and hierarchical merger of small sub-clusters (Longmore et al. 2014; Vázquez-Semadeni et al. 2019; Krumholz et al. 2019; Polak et al. 2023; Zhou et al. 2025). For example, Guszejnov et al. (2022) simulated a molecular cloud of mass  $\sim 2 \times 10^4 M_{\odot}$  and surface density  $\sim 60 M_{\odot} \text{ pc}^{-2}$  and investigated

its evolution over time by considering different physical factors like gas pressure, magnetic field, turbulence, and stellar feedback. The authors found that the cloud is able to form a cluster of mass  $\sim 1.4 \times 10^3 M_{\odot}$  with an efficiency of around 7% in 4 Myr of time through the hierarchical assembly of gas, stars, and sub-clusters, adding relevance to the hierarchical scenario of cluster formation. At around 6 Myr, the feedback starts to affect the cloud significantly and disrupts the cloud in 8 Myr. Although it is still possible to form bound clusters with low SFE, simulations in general suggest that massive bound clusters, in particular the young (less than a few Myr) and compact ones, were most likely formed in regions with high SFEs (e.g. see discussion in [Fujii 2015](#); [Banerjee & Kroupa 2018](#)).

For the studied cluster-forming clumps, the median SFE is found to be somewhat less than 0.3. As discussed above, most simulations suggest a high SFE ( $\geq 30\%$ ) is necessary to form massive bound clusters ([Baumgardt & Kroupa 2007](#); [Kruijssen 2012](#); [Fujii 2015](#)). Thus, if these simulations are to be believed, the low efficiency found in the studied clumps suggests that the clusters within them are unlikely to retain a significant fraction of bound stars as they age. However, we acknowledge that if the dense gas clumps are part of the larger cloud, they may remain gravitationally bound for a longer time with the continuous supply of matter and may continue to form stars. Although stellar feedback is not yet significant in these clusters, the fact that the median disk lifetime of young stars in young clusters is found to be around 2.5 Myr (see discussion in [Rawat et al. 2024a](#), and references therein), implies that the formation of young stars declines significantly beyond 2.5 Myr. Thus, we do not expect a significant rise in the SFE in most of these clusters, although simulations with characteristics of the studied sample are needed to ascertain this hypothesis. Nevertheless, our results point to the fact that the low SFE of the cluster forming clumps in the Galactic plane could be a possible reason for the "infant mortality" inferred from the statistics of embedded to open clusters by [Lada & Lada \(2003\)](#), where a high fraction of young clusters/protoclusters dissolve in the Galactic field, and only a few per cent remain bound. Our results suggest that the formation of massive bound clusters likely requires a special environment, such as the high-pressure conditions expected such as in galactic center or in galaxy mergers or colliding substructures that compress a larger fraction of gas over short timescales (e.g. see discussion in [Kruijssen 2025](#)), rather than the environment studied in this work.

## 5 SUMMARY AND CONCLUDING REMARKS

We present the statistical analysis of a sample of 17 cluster-forming clumps to investigate the relation between star formation rate and gas surface density at the clump scale. We constrained our sample up to a distance of 2.2 kpc for better characterization of cluster properties. The UKIDSS NIR photometric data and *Herschel* dust continuum-based column density maps were used to derive various properties of the clusters, such as extinction, age, stellar and gas mass, SFR, and SFE. The SFRs in our sample range from  $\sim 29$  to  $500 M_{\odot} \text{ Myr}^{-1}$ , with a mean around  $184 M_{\odot} \text{ Myr}^{-1}$ . The instantaneous SFEs range from  $\sim 0.07$  to  $0.51$ , with a mean around  $0.23$ . The mean and median  $\Sigma_{\text{gas}}$  of the clumps is  $\sim 314 M_{\odot} \text{ pc}^{-2}$  and  $\sim 258 M_{\odot} \text{ pc}^{-2}$ , respectively.

We found that  $\Sigma_{\text{SFR}}$  varies with  $\Sigma_{\text{gas}}$  as  $\Sigma_{\text{SFR}} \propto \Sigma_{\text{gas}}^{(1.46 \pm 0.28)}$  in the studied sample of cluster-forming clumps, and both quantities are well correlated. The  $\Sigma_{\text{SFR}} - \Sigma_{\text{gas}}$  relation in this work lies well above most of the previously obtained relations at extragalactic, cloud, and clump scales. The volumetric star formation relation is found to be of the form  $\Sigma_{\text{SFR}} \propto (\Sigma_{\text{gas}}/t_{\text{ff}})^{(0.80 \pm 0.15)}$ , and it also lies above the

previously obtained relations at the cloud scale. The mean  $\epsilon_{\text{ff}}$  of clumps found in this work is around 15%, which is significantly higher than the constant efficiency per free-fall time reported for nearby MCs ([Krumholz & McKee 2005](#); [Krumholz et al. 2012](#)). We suggest that the high values observed in the  $\Sigma_{\text{SFR}}$  vs.  $\Sigma_{\text{gas}}$  and  $\Sigma_{\text{SFR}}$  vs.  $\Sigma_{\text{gas}}/t_{\text{ff}}$  planes for the studied clumps are likely due to the fact that we have studied the scaling relations in compact clumps ( $< 1.6$  pc) with high gas surface densities that are associated with active embedded star clusters. This also implies that star formation scaling relations may not be universal and depend on local conditions, scales, and evolutionary status. Simulations also suggest a higher star-formation rate per free-fall time in compact and dense clouds than fiducial clouds (e.g. [He et al. 2019](#)). Most of the clumps in our sample have  $\Sigma_{\text{gas}} \gtrsim 110 M_{\odot} \text{ pc}^{-2}$ , and the SFR–gas mass relations show a good correlation, which favours the conclusions of [Lada et al. \(2010\)](#), [Heiderman et al. \(2010\)](#), and [Evans et al. \(2014\)](#), that the SFR–gas mass relations become better correlated at higher threshold density.

We find that the median SFE of the cluster-forming clumps is somewhat lower than the expected high SFE required for star clusters to remain bound as they age, as suggested by simulations. Thus, the studied clusters might not survive violent gas expulsions to remain bound for a longer time.

Overall, our results do not favour a universal relation between star formation rate and gas mass that can explain the star formation process across all scales, from galaxies and giant molecular clouds to smaller structures like clouds and clumps.

## ACKNOWLEDGEMENT

We thank the anonymous referee for the useful comments and suggestions to improve the quality of the paper. The research work at the Physical Research Laboratory is funded by the Department of Space, Government of India. D.K.O. acknowledges the support of the Department of Atomic Energy, Government of India, under Project Identification No. RTI 4002. This work makes use of data obtained from the UKIRT Infrared Deep Sky Survey, obtained using the wide field camera on the United Kingdom Infrared Telescope on Mauna Kea. We acknowledge the *Herschel* Hi-GAL survey team and ViaLactea project funded by EU carried out at Cardiff University. We thank Matthew W. Hosek Jr. for all the discussions and support related to the SPISEA code. We are also thankful to Mark Heyer for sharing the data from his work on massive clumps to compare with this work.

## DATA AVAILABILITY

For this study, we have used the NIR photometric data from UKIDSS, which is available on the WFCAM science archive, <http://wsa.roe.ac.uk/>. We have also used the FIR data from *Herschel*, which is available on the archive. The *Herschel* column density maps based on PPMAP are available on the archive, [http://www.astro.cardiff.ac.uk/research/ViaLactea/PPMAP\\_Results/](http://www.astro.cardiff.ac.uk/research/ViaLactea/PPMAP_Results/). The radio data from the NVSS survey used in this work is also available on the archive, <https://www.vla.nrao.edu/astro/nvas>.

## REFERENCES

- Allard F., 2014, in Booth M., Matthews B. C., Graham J. R., eds, IAU Symposium Vol. 299, Exploring the Formation and Evolution of Planetary Systems. pp 271–272, [doi:10.1017/S1743921313008545](https://doi.org/10.1017/S1743921313008545)

- Allen T. S., et al., 2008, *ApJ*, **675**, 491
- Almendros-Abad V., et al., 2023, *A&A*, **677**, A26
- Alves J., Lombardi M., Lada C. J., 2007, *A&A*, **462**, L17
- André P., 2017, *Comptes Rendus Geoscience*, **349**, 187
- Banerjee S., Kroupa P., 2015, *MNRAS*, **447**, 728
- Banerjee S., Kroupa P., 2018, in *Stahler S., ed., Astrophysics and Space Science Library Vol. 1024, The Birth of Star Clusters*. p. 143 ([arXiv:1512.03074](https://arxiv.org/abs/1512.03074)), doi:10.1007/978-3-319-22801-3\_6
- Baumann M., Boch T., Pineau F.-X., Fernique P., Bot C., Allen M., 2022, in *Ruiz J. E., Pierfederici F., Teuben P., eds, Astronomical Society of the Pacific Conference Series Vol. 532, Astronomical Data Analysis Software and Systems XXX*. p. 7
- Baumgardt H., Kroupa P., 2007, *MNRAS*, **380**, 1589
- Bayo A., Rodrigo C., Barrado Y Navascués D., Solano E., Gutiérrez R., Morales-Calderón M., Allard F., 2008, *A&A*, **492**, 277
- Bayo A., et al., 2017, *MNRAS*, **465**, 760
- Bigiel F., Leroy A., Walter F., Brinks E., de Blok W. J. G., Madore B., Thornley M. D., 2008, *AJ*, **136**, 2846
- Boggs P. T., Spiegelman C. H., Donaldson J. R., Schnabel R. B., 1988, *Journal of Econometrics*, **38**, 169
- Bonnell I. A., Bate M. R., 2006, *MNRAS*, **370**, 488
- Burkhart B., Lazarian A., Goodman A., Rosolowsky E., 2013, *The Astrophysical Journal*, **770**, 141
- Casali M., et al., 2007, *A&A*, **467**, 777
- Chauhan N., Pandey A. K., Ogura K., Jose J., Ojha D. K., Samal M. R., Mito H., 2011, *MNRAS*, **415**, 1202
- Chen Y., Li H., Vogelsberger M., 2021, *MNRAS*, **502**, 6157
- Chevance M., Krumholz M. R., McLeod A. F., Ostriker E. C., Rosolowsky E. W., Sternberg A., 2023, in *Inutsuka S., Aikawa Y., Muto T., Tomida K., Tamura M., eds, Astronomical Society of the Pacific Conference Series Vol. 534, Protostars and Planets VII*. p. 1 ([arXiv:2203.09570](https://arxiv.org/abs/2203.09570)), doi:10.48550/arXiv.2203.09570
- Choi J., Dotter A., Conroy C., Cantiello M., Paxton B., Johnson B. D., 2016, *ApJ*, **823**, 102
- Condon J. J., Cotton W. D., Greisen E. W., Yin Q. F., Perley R. A., Taylor G. B., Broderick J. J., 1998, *AJ*, **115**, 1693
- Cutri R. M., et al., 2003, *VizieR Online Data Catalog: 2MASS All-Sky Catalog of Point Sources (Cutri+ 2003)*, *VizieR On-line Data Catalog: II/246*. Originally published in: 2003yCat.2246....0C
- Dale J. E., Ngoumou J., Ercolano B., Bonnell I. A., 2014, *MNRAS*, **442**, 694
- Damian B., Jose J., Samal M. R., Moraux E., Das S. R., Patra S., 2021, *MNRAS*, **504**, 2557
- Das S. R., Jose J., Samal M. R., Zhang S., Panwar N., 2021, *MNRAS*, **500**, 3123
- Deharveng L., et al., 2012, *A&A*, **546**, A74
- Di Francesco J., et al., 2020, *ApJ*, **904**, 172
- Dib S., Piau L., Mohanty S., Braine J., 2011, *Monthly Notices of the Royal Astronomical Society*, **415**, 3439
- Dib S., Helou G., Moore T. J. T., Urquhart J. S., Dariush A., 2012, *The Astrophysical Journal*, **758**, 125
- Dib S., Gutkin J., Brandner W., Basu S., 2013, *MNRAS*, **436**, 3727
- Dib S., et al., 2025, *A&A*, **693**, A51
- Dunham M. K., Robitaille T. P., Evans II N. J., Schlingman W. M., Cyganowski C. J., Urquhart J., 2011, *ApJ*, **731**, 90
- Dutra C. M., Bica E., 2001, *A&A*, **376**, 434
- Dutta S., Mondal S., Jose J., Das R. K., Samal M. R., Ghosh S., 2015, *MNRAS*, **454**, 3597
- Eden D. J., Moore T. J. T., Urquhart J. S., Elia D., Plume R., Rigby A. J., Thompson M. A., 2015, *MNRAS*, **452**, 289
- Elia D., et al., 2013, *ApJ*, **772**, 45
- Elia D., Evans II N. J., Soler J. D., Strafella F., Schisano E., Molinari S., Giannetti A., Patra S., 2025, *arXiv e-prints*, p. [arXiv:2501.14471](https://arxiv.org/abs/2501.14471)
- Elmegreen B. G., 2008, *ApJ*, **672**, 1006
- Evans Neal J. I., et al., 2009, *ApJS*, **181**, 321
- Evans Neal J. I., Heiderman A., Vutisalchavakul N., 2014, *ApJ*, **782**, 114
- Federrath C., Klessen R. S., 2012, *The Astrophysical Journal*, **761**, 156
- Fujii M. S., 2015, *PASJ*, **67**, 59
- Fukushima H., Yajima H., 2021, *MNRAS*, **506**, 5512
- Geen S., Hennebelle P., Tremblin P., Rosdahl J., 2015, *MNRAS*, **454**, 4484
- Geen S., Soler J. D., Hennebelle P., 2017, *MNRAS*, **471**, 4844
- Getman K. V., Feigelson E. D., Kuhn M. A., Bate M. R., Broos P. S., Garmire G. P., 2018, *MNRAS*, **476**, 1213
- Getman K. V., Feigelson E. D., Kuhn M. A., Broos P. S., Garmire G. P., 2019, *AJ*, **158**, 235
- Goodwin S. P., Bastian N., 2006, *MNRAS*, **373**, 752
- Grudić M. Y., Hopkins P. F., Faucher-Giguère C.-A., Quataert E., Murray N., Kereš D., 2018, *MNRAS*, **475**, 3511
- Grudić M. Y., Kruijssen J. M. D., Faucher-Giguère C.-A., Hopkins P. F., Ma X., Quataert E., Boylan-Kolchin M., 2021, *MNRAS*, **506**, 3239
- Grudić M. Y., Guszejnov D., Offner S. S. R., Rosen A. L., Raju A. N., Faucher-Giguère C.-A., Hopkins P. F., 2022, *MNRAS*, **512**, 216
- Gupta S., Jose J., Das S. R., Guo Z., Damian B., Prakash P., Samal M. R., 2024, *MNRAS*, **528**, 5633
- Guszejnov D., Markey C., Offner S. S. R., Grudić M. Y., Faucher-Giguère C.-A., Rosen A. L., Hopkins P. F., 2022, *MNRAS*, **515**, 167
- Gutermuth R. A., et al., 2008, *ApJ*, **673**, L151
- Gutermuth R. A., Megeath S. T., Myers P. C., Allen L. E., Pipher J. L., Fazio G. G., 2009, *ApJS*, **184**, 18
- Gutermuth R. A., Pipher J. L., Megeath S. T., Myers P. C., Allen L. E., Allen T. S., 2011, *ApJ*, **739**, 84
- Gutermuth R., Dunham M., Offner S., 2019, in *American Astronomical Society Meeting Abstracts #233*. p. 367.10
- Hacar A., Clark S. E., Heitsch F., Kainulainen J., Panopoulou G. V., Seifried D., Smith R., 2023, in *Inutsuka S., Aikawa Y., Muto T., Tomida K., Tamura M., eds, Astronomical Society of the Pacific Conference Series Vol. 534, Protostars and Planets VII*. p. 153 ([arXiv:2203.09562](https://arxiv.org/abs/2203.09562)), doi:10.48550/arXiv.2203.09562
- He C.-C., Ricotti M., Geen S., 2019, *MNRAS*, **489**, 1880
- Heiderman A., Evans Neal J. I., Allen L. E., Huard T., Heyer M., 2010, *ApJ*, **723**, 1019
- Henning T., Cesaroni R., Walmsley M., Pfau W., 1992, *A&AS*, **93**, 525
- Heyer M., Gutermuth R., Urquhart J. S., Csengeri T., Wienen M., Leurini S., Menten K., Wyrowski F., 2016, *A&A*, **588**, A29
- Hills J. G., 1980, *ApJ*, **235**, 986
- Hony S., et al., 2015, *MNRAS*, **448**, 1847
- Hosek Matthew W. J., Lu J. R., Lam C. Y., Gautam A. K., Lockhart K. E., Kim D., Jia S., 2020, *AJ*, **160**, 143
- Jose J., Herczeg G. J., Samal M. R., Fang Q., Panwar N., 2017, *ApJ*, **836**, 98
- Kauffmann J., Bertoldi F., Bourke T. L., Evans N. J. I., Lee C. W., 2008, *A&A*, **487**, 993
- Kennicutt Robert C. J., 1998a, *ARA&A*, **36**, 189
- Kennicutt Robert C. J., 1998b, *ApJ*, **498**, 541
- Kennicutt R. C., Evans N. J., 2012, *ARA&A*, **50**, 531
- King I., 1962, *AJ*, **67**, 471
- Könyves V., et al., 2010, *A&A*, **518**, L106
- Könyves V., et al., 2015, *A&A*, **584**, A91
- Krause M. G. H., et al., 2020, *Space Sci. Rev.*, **216**, 64
- Kroupa P., 2001, *MNRAS*, **322**, 231
- Kruijssen J. M. D., 2012, *MNRAS*, **426**, 3008
- Kruijssen J. M. D., 2025, *arXiv e-prints*, p. [arXiv:2501.16438](https://arxiv.org/abs/2501.16438)
- Krumholz M. R., McKee C. F., 2005, *ApJ*, **630**, 250
- Krumholz M. R., McKee C. F., 2020, *MNRAS*, **494**, 624
- Krumholz M. R., Dekel A., McKee C. F., 2012, *ApJ*, **745**, 69
- Krumholz M. R., et al., 2014, in *Beuther H., Klessen R. S., Dullemond C. P., Henning T., eds, Protostars and Planets VI*. pp 243–266 ([arXiv:1401.2473](https://arxiv.org/abs/1401.2473)), doi:10.2458/azu\_uapress\_9780816531240-ch011
- Krumholz M. R., McKee C. F., Bland-Hawthorn J., 2019, *ARA&A*, **57**, 227
- Lada C. J., Lada E. A., 2003, *ARA&A*, **41**, 57
- Lada C. J., Lombardi M., Alves J. F., 2010, *ApJ*, **724**, 687
- Lada C. J., Forbrich J., Lombardi M., Alves J. F., 2012, *ApJ*, **745**, 190
- Lada C. J., Lombardi M., Roman-Zuniga C., Forbrich J., Alves J. F., 2013, *The Astrophysical Journal*, **778**, 133
- Lee E. J., Miville-Deschênes M.-A., Murray N. W., 2016, *ApJ*, **833**, 229
- Li H., Vogelsberger M., Marinacci F., Gnedin O. Y., 2019, *MNRAS*, **487**, 364
- Lombardi M., Lada C. J., Alves J. F., 2013, *A&A*, **559**, A90
- Longmore S. N., et al., 2014, in *Beuther H., Klessen R. S., Dulle-*

mond C. P., Henning T., eds, Protostars and Planets VI. pp 291–314 ([arXiv:1401.4175](https://arxiv.org/abs/1401.4175)), doi:10.2458/azu\_uapress\_9780816531240-ch013

Lucas P. W., et al., 2008, *MNRAS*, **391**, 136

Marsh K. A., Whitworth A. P., 2019, *MNRAS*, **483**, 352

Maud L. T., Moore T. J. T., Lumsden S. L., Mottram J. C., Urquhart J. S., Hoare M. G., 2015, *MNRAS*, **453**, 645

Mège P., et al., 2021, *A&A*, **646**, A74

Méndez-Delgado J. E., Amayo A., Arellano-Córdova K. Z., Esteban C., García-Rojas J., Carigi L., Delgado-Inglada G., 2022, *MNRAS*, **510**, 4436

Molinari S., et al., 2010, *A&A*, **518**, L100

Murray N., 2009, *ApJ*, **691**, 946

Mužić K., Scholz A., Peña Ramírez K., Jayawardhana R., Schödel R., Geers V. C., Cieza L. A., Bayo A., 2019, *ApJ*, **881**, 79

Nayak P. K., Narang M., Manoj P., Gorti U., Subramaniam A., George N., Mondal C., 2024, *ApJ*, **972**, 19

Ojha D. K., et al., 2011, *ApJ*, **738**, 156

Pandey A. K., Samal M. R., Chauhan N., Eswaraiah C., Pandey J. C., Chen W. P., Ojha D. K., 2013, *New Astron.*, **19**, 1

Panwar N., et al., 2017, *MNRAS*, **468**, 2684

Panwar N., Pandey A. K., Samal M. R., Battinelli P., Ogura K., Ojha D. K., Chen W. P., Singh H. P., 2018, *AJ*, **155**, 44

Parker R. J., Wright N. J., Goodwin S. P., Meyer M. R., 2014, *MNRAS*, **438**, 620

Parmentier G., Pfalzner S., Grebel E. K., 2014, *ApJ*, **791**, 132

Patra S., II N. J. E., Kim K.-T., Heyer M., Kauffmann J., Jose J., Samal M. R., Das S. R., 2022, *The Astronomical Journal*, 164, 129

Pineda J. E., et al., 2022, *arXiv e-prints*, p. [arXiv:2205.03935](https://arxiv.org/abs/2205.03935)

Pokhrel R., et al., 2020, *ApJ*, **896**, 60

Pokhrel R., et al., 2021, *ApJ*, **912**, L19

Polak B., et al., 2023, *arXiv e-prints*, p. [arXiv:2312.06509](https://arxiv.org/abs/2312.06509)

Povich M. S., Townsley L. K., Robitaille T. P., Broos P. S., Orbin W. T., King R. R., Naylor T., Whitney B. A., 2016, *ApJ*, **825**, 125

Quireza C., Rood R. T., Bania T. M., Balsev D. S., Maciel W. J., 2006, *ApJ*, **653**, 1226

Rawat V., et al., 2023, *MNRAS*, **521**, 2786

Rawat V., Samal M. R., Ojha D. K., Kumar B., Sharma S., Jose J., Sagar R., Yadav R. K., 2024a, *AJ*, **168**, 136

Rawat V., et al., 2024b, *MNRAS*, **528**, 1460

Rawat V., et al., 2024c, *MNRAS*, **528**, 2199

Rebassa-Mansergas A., et al., 2021, *MNRAS*, **506**, 5201

Rieke G. H., Lebofsky M. J., 1985, *ApJ*, **288**, 618

Rubin R. H., 1968, *ApJ*, **154**, 391

Samal M. R., et al., 2015, *A&A*, **581**, A5

Samal M. R., Deharveng L., Zavagno A., Anderson L. D., Molinari S., Russeil D., 2018, *A&A*, **617**, A67

Schisano E., et al., 2020, *MNRAS*, **492**, 5420

Schmidt M., 1959, *ApJ*, **129**, 243

Schuller F., et al., 2009, *A&A*, **504**, 415

Shukirgaliyev B., Parmentier G., Berczik P., Just A., 2017, *A&A*, **605**, A119

Soderblom D. R., Hillenbrand L. A., Jeffries R. D., Mamajek E. E., Naylor T., 2014, in Beuther H., Klessen R. S., Dullemond C. P., Henning T., eds, Protostars and Planets VI. pp 219–241 ([arXiv:1311.7024](https://arxiv.org/abs/1311.7024)), doi:10.2458/azu\_uapress\_9780816531240-ch010

Sokolov V., et al., 2019, *ApJ*, **872**, 30

Suin P., Zavagno A., Colman T., Hennebelle P., Verliat A., Russeil D., 2024, *A&A*, **682**, A76

Thompson R. I., 1984, *The Astrophysical Journal*, **283**, 165

Vázquez-Semadeni E., Palau A., Ballesteros-Paredes J., Gómez G. C., Zamora-Avilés M., 2019, *MNRAS*, **490**, 3061

Vutisalchavakul N., Evans Neal J. I., Heyer M., 2016, *ApJ*, **831**, 73

Willis S., Guzman A., Marengo M., Smith H. A., Martínez-Galarza J. R., Allen L., 2015, *The Astrophysical Journal*, **809**, 87

Wu J., Evans N. J., Shirley Y. L., Knez C., 2010, *The Astrophysical Journal Supplement Series*, **188**, 313

Yadav R. K., et al., 2022, *ApJ*, **926**, 16

Zamora-Aviles M., et al., 2024, *arXiv e-prints*, p. [arXiv:2409.11588](https://arxiv.org/abs/2409.11588)

Zavagno A., et al., 2010, *A&A*, **518**, L81

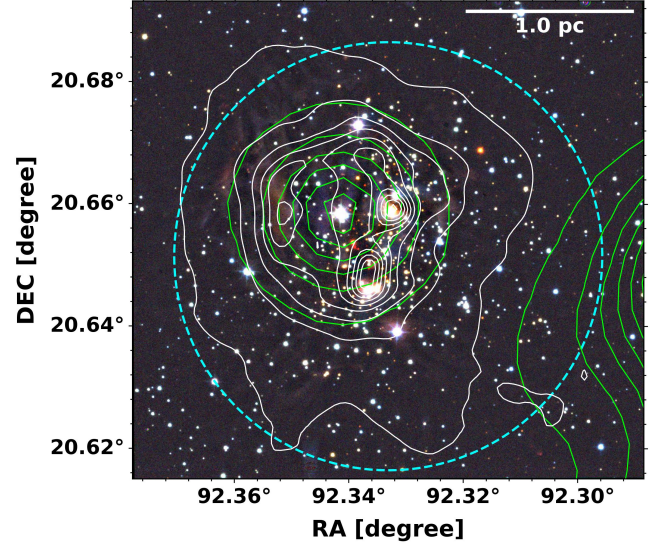


**Figure A1.** UKIDSS color-composite image of IRAS 06063+2040 over which the contours of ionized emission at 1.46 GHz and 70  $\mu\text{m}$  emission are shown by green and white colors, respectively. The contour levels are shown above  $5\sigma$  from the background.

Zhou J.-w., Kroupa P., Dib S., 2024a, *A&A*, **688**, L19

Zhou J.-w., Dib S., Kroupa P., 2024b, *A&A*, **691**, A293

Zhou J. W., Dib S., Kroupa P., 2025, *arXiv e-prints*, p. [arXiv:2501.08831](https://arxiv.org/abs/2501.08831)

Zinchenko I., Liu S. Y., Su Y. N., Kurtz S., Ojha D. K., Samal M. R., Ghosh S. K., 2012, *ApJ*, **755**, 177

Zinchenko I., Liu S.-Y., Su Y.-N., Wang Y., 2018, *Research in Astronomy and Astrophysics*, **18**, 093

de los Reyes M. A. C., Kennicutt Robert C. J., 2019, *ApJ*, **872**, 16

## APPENDIX A: IONIZED GAS PROPERTIES OF THE CLUMPS

Fig. A1 shows the 1.46 GHz radio emission and 70  $\mu\text{m}$  emission over the UKIDSS image of IRAS 06063+2040. To calculate  $N_{\text{Lyc}}$  from  $S_\nu$ , we used the following relation (Rubin 1968)

$$N_{\text{Lyc}} = 4.76 \times 10^{48} \left( \frac{S_\nu}{\text{Jy}} \right) \left( \frac{T_e}{\text{K}} \right)^{-0.45} \left( \frac{\nu}{\text{GHz}} \right)^{0.1} \left( \frac{d}{\text{kpc}} \right)^2, \quad (\text{A1})$$

where  $T_e$  is the electron temperature,  $\nu$  is the frequency of the radio emission, and  $d$  is the distance to the clumps. We adopted an average value of  $T_e$  to be around  $8200 \pm 240$  K from Quireza et al. (2006). Using  $N_{\text{Lyc}}$  and the masses and sizes of the clumps, the radiation and gravitational pressure forces for the clumps can be derived as (Murray 2009)

$$F_{\text{rad}} = 5 \times 10^{34} \left( \frac{L}{4 \times 10^{11} L_\odot} \right) \text{dyn}, \quad (\text{A2})$$

$$F_{\text{grav}} = 3 \times 10^{34} \left( \frac{M}{10^9 M_\odot} \right)^2 \left( \frac{1 \text{kpc}}{R} \right)^2 \text{dyn}, \quad (\text{A3})$$

where  $L$  is the luminosity of the ionizing source. We have taken the luminosity values corresponding to the Lyman continuum photons given in Thompson (1984).

## APPENDIX B: AGE DETERMINATION FROM SED MODELLING

In order to validate the age estimation of the clusters from KLF modelling, we accessed the age of IRAS 06063+2040 using SED modelling. We used VOSA (VO Sed Analyzer; Bayo et al. 2008) tool, which has been effectively used to derive the stellar properties of young stars (e.g. Mužić et al. 2019; Almendros-Abad et al. 2023; Gupta et al. 2024). VOSA compares the observed fluxes with the synthetic photometry, looking for the best-fit effective temperature ( $T_{\text{eff}}$ ), extinction ( $A_V$ ), and surface gravity ( $\log(g)$ ) combination. For fitting, in addition to UKDISC data, we used optical to NIR data from GAIA DR3, Pan-STARRS, *Spitzer*, and WISE, as available in the Vizier. We used the distance  $2.2 \pm 0.2$  kpc, the BT-Settle atmospheric models (Allard 2014),  $T_{\text{eff}}$  over the range of 1000–7000 K, and  $A_V$  as  $6 \pm 3$  mag. For objects showing excess in *Spitzer* photometry, SED fitting is performed over the shorter wavelengths; otherwise, the full available range is included in the fit. We used the  $\log(g)$  between 3.5 and 5.0, which is suitable for young low-mass stars and the field stars; however, we note that the VOSA SED fitting procedure is largely insensitive to  $\log(g)$  (see Bayo et al. 2017). In fact, we find that, in general, the fits are not significantly affected by variations in  $\log(g)$ . With the aforementioned approach, we derived effective temperatures and luminosities for the sources. The radii of our objects are calculated using the Stefan-Boltzmann equation, making use of the luminosities and effective temperatures previously computed by VOSA. With the derived stellar parameters, VOSA also provides the age of the sources based on their position on the HR diagram using theoretical isochrones. To determine the age of the cluster, we keep only those sources with good SED fitting, i.e. sources with  $Vgfb$  value less than 15.  $Vgfb$  is a modified reduced  $\chi^2$ , calculated by forcing that the observational errors are, at least, 10% of the observed flux. In general,  $Vgfb < 15$  is usually considered as a proxy for well-fitted SEDs (e.g. Rebassa-Mansergas et al. 2021; Nayak et al. 2024). We further remove the foreground sources from the sample by selecting sources whose  $J-H$  and  $H-K$  colors are less than 0.8 and 0.25 mags, respectively. To identify foreground sources, we compared the NIR color-color diagram of the cluster population with that of the control field population, as described in Rawat et al. (2024a), and selected sources based on this comparative analysis. With the aforementioned criteria, we are left with only 15 sources, whose median age was found to be  $0.8 \pm 0.4$  Myr. Figure B1 shows an exemplary SED fitted with VOSA.

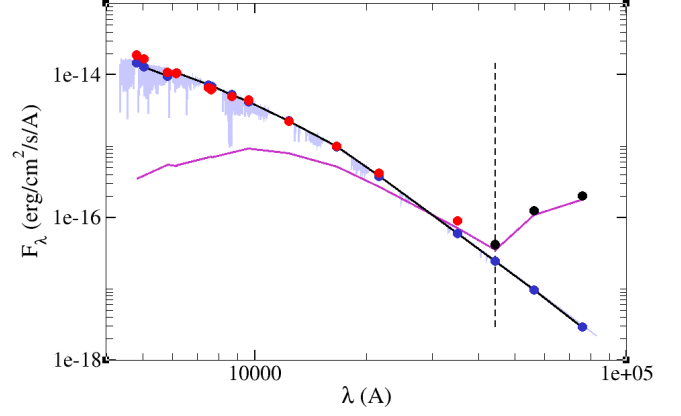


**Figure B1.** Example of a SED fitting as generated by VOSA for IRAS 06063+2040. The blue spectrum represents the theoretical model that fits best, while red dots represent the observed photometry. The black dots are affected by IR excess and are not considered in fitting.

This paper has been typeset from a  $\text{\TeX}/\text{\LaTeX}$  file prepared by the author.